The Pennsylvania State University

The Graduate School

John and Willie Leone Family Department of Energy and Mineral Engineering

EVALUATION OF FLUID TRANSPORT PROPERTIES OF COAL BED METHANE RESERVOIRS

A Dissertation in

Energy and Mineral Engineering

by

Dennis Arun Alexis

Submitted in Partial Fulfillment
of the Requirements
for the Degree of

Doctor of Philosophy

August 2013

The dissertation of Dennis Arun Alexis was reviewed and approved* by the following:

Zuleima T. Karpyn
Associate Professor of Petroleum and Natural Gas Engineering
Quentin E. and Louise L. Wood Faculty Fellow in
Petroleum and Natural Gas Engineering
Dissertation Co-Advisor
Co-Chair of Committee

Turgay Ertekin
Professor of Petroleum and Natural Gas Engineering
George E. Trimble Chair in Earth and Mineral Sciences
Dissertation Co-Advisor
Co-chair of Committee

John Yilin Wang
Assistant Professor of Petroleum and Natural Gas Engineering

Derek Elsworth
Professor of Energy and Geo-Environmental Engineering

Demian Saffer
Professor of Geosciences

Luis F. Ayala H.
Associate Professor of Petroleum and Natural Gas Engineering
Associate Department Head for Graduate Education

*Signatures are on file in the Graduate School

ABSTRACT

Determination of petro-physical properties of coal bed methane (CBM) reservoirs is essential in evaluating a potential prospect for commercial exploitation. In particular, permeability is the most significant rock property controlling the transport of natural gas to the wellbore. Specifically, relative permeability of coal to gas and water in the fracture network determines the ease with which immiscible fluids travel through the reservoir in the presence of each other and directly impacts the amount of hydrocarbons that can be ultimately recovered. Due to the complex and heterogeneous nature of coal seams, proper relative permeability relationships are needed to accurately describe the transport characteristics of coal for reservoir modeling and production forecasting. In this work, absolute and relative permeability of different coal samples were determined experimentally under steady-state flowing conditions. Multiphase flow tests were conducted using brine, helium and carbon dioxide as the flowing phases under different magnitudes of confining and pore pressures. Results indicate that effective stress (Confining pressure – average pore pressure) has a significant effect on both absolute and relative permeability of coal. With increases in effective stresses, the absolute permeability decreases. Effective permeability and relative permeability, as well as the cross over point and the width of the mobile two-phase region decrease as the effective stress increases. In addition, the mobile range of gas and water in the coal samples investigated corresponds with water saturations above 50%, irrespective of the base absolute permeability of the sample. In brine-carbon dioxide two-phase flow experiments, the effect of carbon dioxide adsorption was observed as effective permeabilities measured decreased in comparison to the helium-brine permeabilities at the same flowing ratios. Gas transport is restricted in the presence of water as significant water occupation is observed in the fracture network during the two phase flow tests and also evident from the magnitude of the effective and relative permeabilities. As a result, relative permeability

characteristics of CBM systems were found to be insufficiently represented as sole functions of fluid saturation. In addition, laboratory measurements were used to conduct field scale simulations of primary recovery from CBM systems using variable, stress-dependent relative permeabilities. Simulation results show that methane recovery from CBM reservoirs can be overestimated when dynamic changes in relative permeability relationships are ignored. A multi-dimensional correlation between relative permeability, fluid saturation and specific surface area of the cleat network is proposed as a continuation from this work in order to account for stress-related changes in cleat network connectivity.

TABLE OF CONTENTS

LIST OF FIGURES

LIST OF TABLES

ACKNOWLEDGEMENTS

During the last six years or so at Penn State I have had the opportunity to learn and grow from a variety of experiences. I would like to express my heartfelt thanks to The Pennsylvania State University, the Directorate of International Student and Scholar Advising (DISSA), The John and Willie Leone Family Department of Energy and Mineral Engineering, The EMS Energy Institute and the Center for Quantitative X-ray Imaging (CQI) for being an integral part in all my achievements here.

I would like to express my deepest sense of appreciation and gratitude to my advisors, Dr. Zuleima Karpyn and Dr. Turgay Ertekin for investing their time and effort in educating and supporting me all these years in many different ways and without a doubt I have learnt many things from them. I would also like to thank Dr. Luis F Ayala who always wished the best things for me and for also giving me the opportunity to work with him for my Master's degree. Special thanks to Dr. Joel Haight for his insightful opinions about important decisions that I had to make. My sincere appreciation goes towards my committee members, Drs. Derek Elsworth, John Wang and Demian Saffer for agreeing to be in my dissertation committee and also for their time. Also, I would like to thank Dr. Jonathan Mathews for his inputs related to the behavior of coal. Thanks to Ken Biddle and his team at the EMS Machine shop for his assistance in fabricating/modifying the necessary pieces of equipment for conducting experiments. Gary Mitchell's in depth coal petrographic analysis is greatly appreciated. Dustin Crandall's help related to providing coal samples and with coal coring at NETL, Morgantown and his ever enthusiastic communication whenever I wrote to him is just something I will never forget. Dr. Larry Grayson's help in procuring coal blocks and Pete Merritts's (Alpha Natural Resources) and Ed Ratays's (Amfire Mining Company) assistance in getting suitable coal blocks are greatly appreciated.

This research effort would not have been possible without the financial support of NETL, Morgantown, John and Willie Leone Family Department of Energy and Mineral Engineering and the Quentin and Louise Wood Fellowship and it is gratefully acknowledged. Having done mostly experimental work, I would also like to thank Dr. Phil Halleck who always has been really kind to devote his time and knowledge to give us many ideas to effectively overcome all the challenges in the laboratory. Tim Stecko's help with using the X-ray CT scanner is greatly appreciated. Also, I would like to thank Dr.Tim Ryan for helping me understand the concepts related to X-ray CT imaging. A special thanks to my colleagues, Erhan Aslan, Burak Kulga and Hemant Kumar for the modeling and experimental related discussions. Also, I would like to thank Donna Marcotte of Huntingdon, PA who was greatly responsible in helping me professionally with my resume and also providing me with subsequent networking opportunities. George Vassilellis, Ole Engels and Charles Li of Gaffney, Cline & Associates are greatly appreciated for giving me the maiden opportunity to work in the oil and gas consulting industry through an internship experience.

It would not have been possible to fully participate and successfully complete my studies without the unfaltering support, understanding and prayers of my family members, especially my parents and grandmother. I am ever indebted to them for standing by me during all the moments and constantly encouraging me to keep going. I also thank my friends, colleagues and well-wishers near and far who have helped me and have contributed in one way or the other to complete my academic journey at Penn State. I wish them well in all their endeavors now and hereafter.

Finally, I would like to thank the Kennis family of Sykesville, PA for accommodating me as one in their family over the last couple of years and giving me a home to stay whenever I went to visit them and their affection and warmth will linger in my mind throughout my life.

NOMENCLATURE

P_{eff}	Effective Stress (psi)
k_{weff}	Fracture effective permeability to water (mD)
k_{geff}	Fracture effective permeability to gas (mD)
k_{rg}	Fracture relative permeability to gas
k_{rw}	Fracture relative permeability to water
k_{abs}	Absolute permeability of coal (mD)
P_{conf}	Confining pressure (psi)

Chapter 1

BACKGROUND

Producing methane from coal seams has been practiced for more than half a century and successful commercial exploitation of coal bed methane systems has been witnessed on a global scale, especially in the United States. It is estimated that the global methane reserves from coal seams can be up to 9,500 Tcf and in the US up to 3,000 Tcf (Olsen et al., 2003). Coal seams that are deep and uneconomical to mine are potential candidates for storage of CO_2 due to its high affinity to adsorb CO_2, thus enhancing methane recovery (Pekot & Reeves, 2003). Hence research interest has increased in the recent past to study and understand the behavior of different types of coals for long term reservoir monitoring and management.

Coal seams are dual porosity, naturally fractured systems and fall under the category of unconventional hydrocarbon reservoir formations as gas is generated and stored in an adsorbed form in the matrix, which has very low permeability. The so-called primary porosity of CBM systems corresponds to the micro pores (< 2 nm) which are present in the coal matrix, while the secondary porosity is due to the macropores or the cleats (natural fracture network) (> 5 nm). In the natural state, approximately 90% of methane is present in a highly adsorbed state in the micropores within the matrix (Hall et al., 1994). When the pressure in the cleats or the fractures is reduced, methane first desorbs from the micropores and diffuses into the fractures under Fickian diffusion and once the methane reaches the cleats, the flow in the fractures is primarily driven by the pressure gradient described by Darcy's law. For that reason, CBM reservoirs are considered to be multi-mechanistic transport systems (King et al., 1983; Ertekin et al., 1988; Ertekin & Sung, 1989). Generally, when gas desorbs from the micropores, the matrix shrinks which leads to an increase in permeability (Harpalani & Shraufnagel, 1990) and when gas adsorbs, the permeability decreases due to matrix swelling. In an Enhanced Coal Bed Methane (ECBM)

Recovery/Sequestration setup where CO_2 is injected to displace methane, it can be seen that adsorption and desorption of gases can occur simultaneously, leading to a multi-component sorption/desorption scenario (Katyal et al., 2007). Hence the interaction of gases with the observed changes in coal permeability accompanied by shrinkage/swelling characteristic of coal is a complex phenomenon.

In general, absolute permeability (k_{abs}) is a measure of the ability of a porous medium to transmit a fluid through its interconnected pores when the medium is 100% saturated with that fluid. When two or more fluids flow together, the ability of the rock to transmit each fluid is different such that the relative permeability (k_r) of the porous medium to the flowing fluids becomes important. In two-phase flow conditions for flowing phases *i* and *j*, we can write the flow rate of each phase (q) with dynamic viscosity (μ) based on Darcy's law as follows:

$$q_i = -\frac{k_{eff\,i}}{\mu_i} A \frac{\Delta P_{eff_i}}{\Delta L}$$

$$q_j = -\frac{k_{eff\,j}}{\mu_j} A \frac{\Delta P_{eff_j}}{\Delta L}$$

Here A is the sample's cross-sectional area, ΔL is the sample length, and ΔP_{effi} is the differential pressure across the sample at the particular q_i. Hence, the relative permeability of the porous medium to phases i and j can be written as

$$k_{r_i} = \frac{k_{eff_i}}{k_{abs}}; k_{r_j} = \frac{k_{eff_j}}{k_{abs}}$$

Here $k_{eff\,i}$ is the effective permeability of phase *i*. As will be shown, $k_{eff\,i}$ is an appropriate parameter to describe the multiphase motion of the phases through fractured coal. This is primarily due to the tendency of the coal matrix to deform under external forces.

Since relative permeability has a first order dependency on saturation (Honarpour and Mahmood, 1988), Figure 1.1 shows the traditional way of representing relative permeability characteristics as a unique function of saturation and is provided as one of the inputs to numerical models. Here k_{rw} and k_{rg} are the relative permeabilities of the rock to the flow of water and gas.

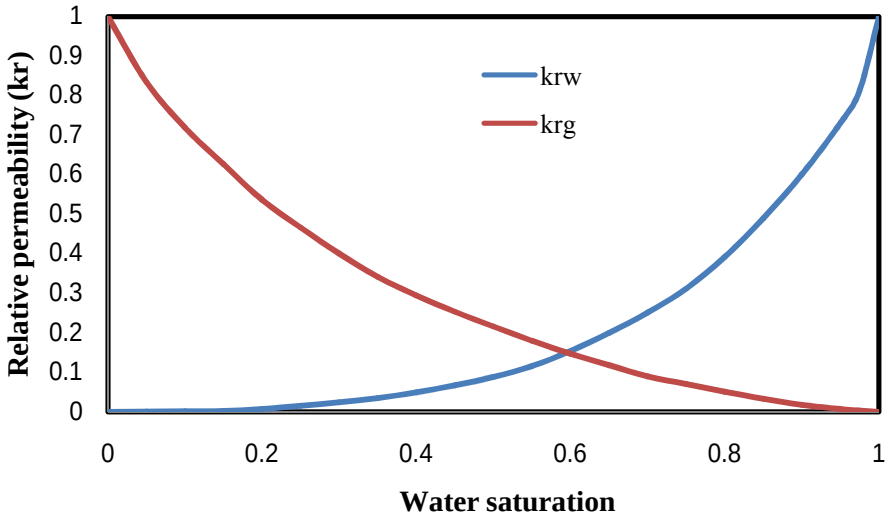

Figure 1-1. Typical representation of gas and water relative permeabilities

With respect to coal, "Relative permeability is one of the most important parameters affecting production from coalbed methane reservoirs" (Harpalani & Shraufnagel, 1990). Clarkson et al. (2010) observe that primary gas production from CBM reservoirs is significantly dependent on the relative permeability of coal to gas and water and also in the enhanced recovery of methane by CO_2 injection. Hence relative permeability of coal to gas and water is a significant parameter for coal bed methane models.

Historically, research investigations with respect to coal seams for reservoir engineering applications have focused on permeability determination/evolution studies accounting for geo-mechanical/ swelling/ shrinkage effects, gas absorption/desorption studies, relative permeability determination, numerical modeling and well test analysis and material balance and production decline analysis. Among these, research investigations aimed at understanding the relative

permeability characteristics of coal seams which primarily describes the flow of water and gas in the cleat or the fracture network has been very minimal.

Permeability of coal to gas and water was carried out by Dabbous et al. (1973) on Pittsburgh and Pocahontas 1.5" diameter coal samples using air and water separately. About 40% of the 35 Pittsburgh samples had an absolute air permeability in the range of 1 – 10 mD and about 60 % of the 28 Pocahontas samples had air permeability in the range of 0.1 – 1 mD. A constant over burden pressure of 200 psi was used for these measurements. The water absolute permeability of the samples were between the range of 0.069 mD to 167 mD for the Pittsburgh samples and for the Pocahontas samples they were in the range of 0.08 mD to 20 mD. These measurements were done at a constant overburden pressure of 400 psi. In general, the permeability change with variation in overburden stress was studied and they found that as the overburden stress increased, the permeability decreased considerably decreased. These samples also exhibited strong hysteresis effect. It was also observed in some Pocahontas samples, the absolute permeability to water was higher than the corresponding absolute permeability to air due to shear fracturing caused by the flow of water.

Reznik et al. (1974) reported the two phase data obtained by extension of the work done by Dabbous et al. (1973) on Pittsburgh and Pocahontas coals and these measurements were the first reported relative permeability measurements on coals. The stationary phase method and the steady state method were used and both drainage and imbibitions relative permeabilities were measured. In the stationary phase method, the Pittsburgh samples (k_{abs} (0.02 mD - 12.5 mD)) exhibited higher irreducible water saturation during the drainage cycle but the relative permeabilities were similar with relative permeability to gas reaching as high as 1. The Pocanhontas samples (kabs (0.09 mD - 12 mD)) had a similar behavior but the irreducible water saturation was about 20% and 60% on an average.

The effect of overburden pressure on gas and water permeabilities (imbibition and drainage cycles) on six Pittsburgh seam and four Pocahontas coal samples were also measured. For the Pittsburgh samples, the imbibition relative permeability to gas decreased as the overburden pressure increased and covered a wider saturation range for the lowest overburden pressure. The corresponding drainage gas relative permeabilites were higher but no general behavior was observed with respect to overburden pressures as they were more or less the same. The maximum relative permeability to gas reached 1 in both the cases. When compared on an effective permeability basis, the permeability to gas was lower at higher overburden pressures on both drainage and imbibition cycles with the span of the saturation region decreasing as overburden pressures increased. The drainage relative permeability to water decreased as the overburden pressure increased but the imbibition water permeabilities increased with increase in overburden pressure.

For the Pocahontas samples, the relative permeability to gas did not show any notable behavior with the overburden stress with the curves being similar at different overburden pressures with drainage gas relative permeabilites being higher in comparison to the imbibition permeabilities. The saturation span was similar for the drainage and imbibitions cycles with the highest gas relative permeability reaching 1. The relative permeability to water was greater during imbibition in comparison to the drainage measurements and in general showed less variation with overburden pressure changes in comparison to the corresponding gas relative permeabilities. Overall from these two studies, the saturation measurements were reported satisfactory.

Several other relative permeability measurements followed in the next three decades where coal samples from the San Juan basin, Black warrior basin, Australian basins, Canadian basins and Chinese basins were used. In these studies either the steady state or the unsteady state or both the techniques were employed.

San Juan basin and Black Warrior basin

The relative permeability of coal to gas always had a maximum value of 0.1 irrespective of the base absolute permeability of the sample obtained from a particular well in the Fruitland coal seam of the San Juan Basin (Jones et al., 1988). The steady state method was used to determine the gas water relative permeabilities.

Relative permeabilities of coal to gas and water was measured in 3.5" diameter samples from coal cores obtained from Igancio coal seam and the Jagger coal seam of the San Juan Basin and the Black Warrior basin respectively (Puri et al., 1991). Results showed that the maximum relative permeability to gas was 0.94 and 0.68 with the highest irreducible water saturation in the cleat network about 70%. The unsteady state method was used and the results reported were satisfactory.

In a different study, four separate whole core samples obtained from San Juan basin (3) and the Black Warrior basin (1) (diameters of 3. 5" and 2" respectively) were used in the analysis (Gash, 1991). The relative permeability to gas varied between with 0.6 to 0.95 with a corresponding gas saturation of 80%. Comparison between relative permeabilities obtained from the steady and the unsteady state method, showed greater differences with respect to gas in comparison to water. The unsteady state measurement brought in some uncertainties with respect to dead volume measurements. It was concluded that the results obtained from both the methods were comparable within the margin of experimental error of the saturations measurements. Although a variation in absolute permeability due to migration of fines, with time was observed, the relative permeabilities did not change significantly.

The effect of cleat orientation of coal and applied confining stress on relative permeabilities was experimentally investigated on 3.5" samples obtained from La Plata mine in

the San Juan basin using the unsteady state method. (Gash et al., 1992). Similar to the previous study it was observed that the absolute permeabilities changed due to migration of fines and also when the flow direction was changed. It was concluded that as the overburden stress increased the relative permeability to water decreased more in comparison to the relative permeability to gas, but this observed change was very small. Cleat orientation did not have any effect on the measured absolute or relative permeabilities.

In a different study (Hyman et al., 1992), two-phase tests (steady and unsteady state) were done on cylindrical coal samples obtained from San Juan and the Black Warrior basins. Though the results obtained from both the methods were similar, the relative permeability to gas was significantly different. They concluded that steady state and the unsteady methods had their own limitations with respect to the assumptions and this could be a possible reason for the differences observed as the assumptions may not hold true for coal's heterogeneous structure.

Australian basins

Paterson et al. (1992) measured the relative permeability curves by the unsteady state method on coal sample from the Bowen basin. They observed in their experiments, the water saturation in the samples remained always high leading to a low relative permeability to gas. They concluded that, small sample size, low absolute permeability and mineralization could have contributed to the problem.

Relative permeabilities of coal to methane and water were measured using the unsteady state method in samples (2.5" diameter) from CBM reservoirs (Shedid & Rahman, 2009). The base absolute permeabilities of the samples were 0.013mD, 0.14 mD, 0.262 mD. The highest and lowest gas relative permeability was 0.15 and 0.6 respectively. The gas relative permeability was lower in comparison to the water relative permeability in all three cases. The highest gas permeability and highest irreducible water saturation was observed for the sample with a base permeability of 0.013 mD. No specific trend on relative permeability behavior could be

identified with respect to the base absolute permeability, span of two-phase flow region or the phase cross over points.

Canadian Basins

Relative permeability measurements were done using the unsteady state method on samples (3" diameter) obtained from the Alberta Horseshoe Canyon and Saskatchewan Manville coal deposits (Ham & Kantzas, 2011). The base absolute permeability of the samples were low and in the range of 0.07 mD. Drainage and imbibition relative permeability of coal to gas and water were determined using helium, methane and CO_2 as the gaseous phases with operating pressures reaching upto 300 psi at room temperature. In one of the samples, the relative permeability to gas progressively decreased when the gases were changed from He to CH_4 to CO and was about 0.2 for both the imbibitions and drainage experiments. In the other sample, during the drainage run the relative permeability to gas was about 0.1, but during the imbibition runs, the relative permeability to gas increased when the gases were changed from He to CH_4 to CO_2 reaching as high as 0.8. It was concluded that the coal samples behaved differently with respect to the different gases used as their properties continously changed and a generalization could not be made with respect to the effect of pressure on relative permeability curves as it was complex phenomenon.

Chinese basins

Shen et al. (2011) measured relative permeability characteristics of coals of different ranks from the south Qinshui basin in China using the unsteady state method. It was observed that the relative permeability to gas was consistently lower (0.2 – 0.4) in all the coal samples with narrow range of the two phase flow region and the effective permeability to gas was lower even at irreducible water saturation conditions. Correlations were also developed to relate relative permeabilities as a function of saturation using the power law relationship.

From the studies listed above, over the last three decades there has been very limited and reported experimental work (~10) to determine relative permeability characteristics of coal samples. As samples were from different basins all over the world, the experimental results showed a wide variation (even among samples in similar basins) influenced by the methods employed to determine them and also by the inherent heterogeneous nature of the sample itself. Hence in this work, experimental determination of relative permeability of different coal samples, primarily obtained from the Appalachian basin will be done, to obtain more experimental data and to benchmark experiments. This would help us to extend the current knowledge that would allow us to represent relative permeability characteristics of coal as multi-dimensional quantities as opposed to single functions of saturation.

Chapter 2

PROBLEM STATEMENT

Naturally fractured formations undergo greater structural changes with changes in stress in comparison to non-fractured formations (Duan et.al., 1998). Change in elasticity of the rock combined with variations in fracture apertures make naturally fractured reservoirs more sensitive to stress changes (Warpinski, 1991). Coal being a naturally fractured formation also exhibits strong dependence of permeability on stress conditions (Palmer & Mansoori, 1996; Pan et al., 2010). Effective stress, which is the difference between the overburden stress and the pore pressure, is the one that actually controls the permeability and coal's permeability is strongly affected by effective stress (Connell et al., 2010)

Due to the sorption of fluids in the coal matrix, coal swells or shrinks leading to a decrease or increase in the absolute permeability of coal. This swelling/ shrinkage phenomenon combined with changes in permeability due to effective stress changes, can lead to a net increase or decrease in the absolute permeability depending on which effect dominates. To predict the behavior of coal's absolute permeability with respect to sorption/effective stress variation, several models have been developed (Harpalani & Chen, 1995; Seidle & Huitt, 1995; Palmer & Mansoori, 1996; Levine, 1996; Shi & Durucan, 2005; Robertson & Christiansen, 2007).

Although coal's absolute permeability variation with effective stress/sorption phenomena has been well studied and understood (Harpalani & Chen, 1995; Seidle & Huitt, 1995; Palmer & Mansoori, 1996; Levine, 1996; Shi & Durucan, 2005; Robertson & Christiansen, 2007) the relative permeability behavior of coal in response to changes in effective stress/sorption phenomena is difficult to predict. Moreover, current CBM models (dual porosity models) use

relative permeability relationships for describing the flow of water and gas in the fracture network as a function of saturation alone. In some cases, they are even represented as straight lines implying that permeability is a linear function of saturation. Representation of relative permeabilities as functions of saturation alone may be applicable if they are used to model a conventional non-fractured hydrocarbon reservoir where variability of permeability to changing in-situ stress conditions is minimal during depletion. Furthermore, relative permeability relationships are hysteretic in nature and non- unique as they are affected by saturation history (drainage and imbibition cycles). To address this non-unique nature of relative permeabilities, relative permeability curves have been represented as surfaces, functions of saturation and specific interfacial area in porous media (Haasanizadeh & Gray, 1993a; V Joekar-Niasar et al., 2008). Coal's inherent heterogeneity can add to already non-unique nature of relative permeabilities, thus making the interpretation more complex.

Therefore more experimental investigation is needed that explicitly determines the effect of effective stress on the transport of water and gas in the coal fractures. The major objectives of the work done in this study are as follows:

1. Measure the relative permeability of coal to gas and water in a closed loop circulation system using the steady-state experimental technique.
2. Identify the effect of effective stress on the flow of gas and water under controlled stress and temperature conditions using helium – brine as the flowing phases.
3. Identify how the relative permeability changes in comparison to the helium-brine measurements, when CO_2 – brine is used
4. Conduct simulation studies to illustrate the effect of stress dependent relative permeabilities on the primary recovery of methane.

Understanding the dependence of relative permeabilies on effective stress can pave the way to better represent the relative permeability behavior as multidimensional functions. The

significance of a multi- dimensional relative permeability relationship is that it will provide a more realistic representation to predict the flow of gas and water under the influence of stress and saturation fields for fractured formations like coal seam reservoirs.

Chapter 3

EXPERIMENTAL METHODOLOGY

Samples

The samples used in the present study are coal cores obtained from bituminous coal seams in Marshall County, West Virginia and from a coal processing plant in Clearfield, PA. A total of 5 different samples were used for the experiments and their general characteristics are shown in Table 3.1. Four of these samples were retrieved from wells drilled by CONSOL Energy Inc. in 2010 at depths of 600ft to 700ft. The mean maximum vitrinite reflectance (R_{max}) of these four samples is 0.75% and based on the ASTM coal rank classification scheme they can be classified as high volatile A bituminous coals. The procedures and detailed results of the proximate and petrographic analysis are described in the Appendix.

Table 3-1. Characteristics of samples used in the study

Sample #	**Rank**	**Dimensions**		**Stimulated**
		Diameter(inch)	Length(inch)	
1	High Volatile A Bituminous	2	2.8	No
2	High Volatile A Bituminous	2	3.25	Yes
3	High volatile A Bituminous	2	5	Yes
4	High Volatile A Bituminous	2	4	Yes
5	Not Analyzed	2	4	Yes

Sample stimulation

Except for sample 1, the rest of the coal samples had to be artificially fractured to create an appreciable fracture network for conducting gas and water flow. To induce fractures in the samples, the sample was confined in a C- clamp on both ends and placed between the end jaws of the Brazilian tensile strength (BTS) test machine as shown in figure 3.1. Compressive stress on the sample was loaded progressively until the first induced crack happened.

Figure 3-1. Compressive loading on the sample in a Brazilian tensile strength testing machine

The sample was X-ray CT scanned to determine the effectiveness of the fractures created and figure 3.2 shows the resultant image at a particular location in the sample.

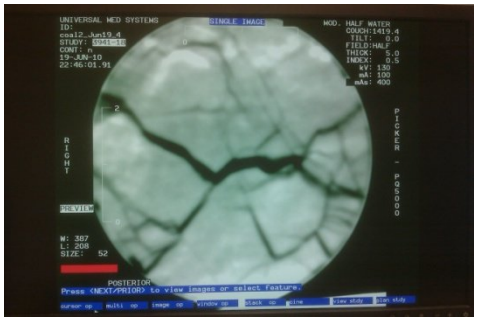

Figure 3-2. X-ray CT image of sample at a particular location in the sample in the axial direction

As seen in figure 3.2, the induced fracture aperture can be very large and this method may not be effective without precise control when operating the BTS test machine. The next attempt was to put the coal inside a heat shrink tube, shrink the tube , axially confine by a C- clamp (figure 3.3), then using a pick hammer to impact the sample with about 5 lbs of force and repeat the same procedure, till the total surface was covered by rotating the sample. The distribution of the fractures created by this second attempt is shown in figure 3.4. One can see here the sample is secure with the fractures propagating in different directions and there is no appreciable deformation. It appears, in this method that we have more control in creating the fractures without affecting the integrity of the sample. Hence this method was used for the other samples.

Figure 3-3. Manual stimulation using pick hammer with sample confined in a C- clamp

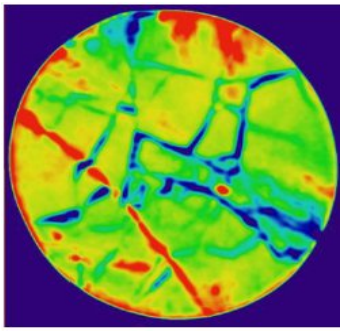

Figure 3-4. X-ray CT image of sample at a particular location in the sample in the axial direction after using the manual method

Experimental set up and procedure

In general relative permeability measurements in the laboratory are done either by using the steady state or the unsteady state method. In the steady state method, the fluids are injected at specific flow-rates and the pressure drop due to these phases is recorded at steady state conditions. The relative permeability of the rock sample to these phases is then determined by employing Darcy's law knowing the absolute permeability of the sample. In the unsteady state technique, typically the non-wetting phase displaces the wetting phase which the porous medium is initially saturated with. Based on the effluent volumes and the pressure measurements, the relative permeabilities are indirectly calculated using the Johnson, Bossler and Naumann (1959) method. Unsteady state tests are faster to perform but steady state tests though need longer time scales, generate more reliable data.

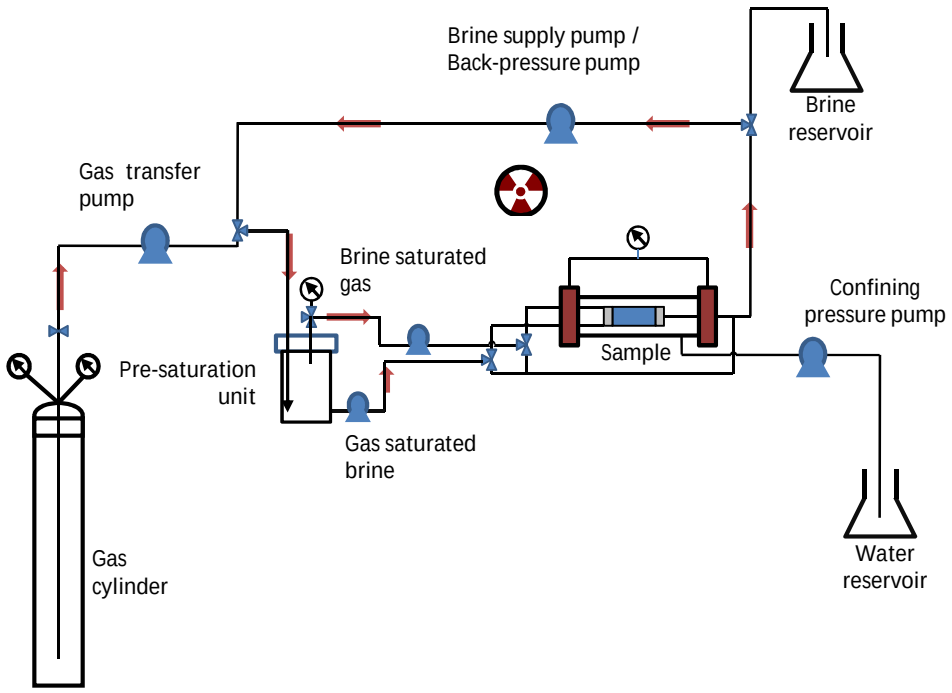

Figure 3-5. Experimental design for single/multiphase flow tests

Figure 3.5 shows the experimental set up for conducting flow experiments. Gas and brine are taken into the 'Pre – saturation unit' which is a pressure vessel capable of being operated up to a maximum pressure and temperature of 3000 psi and 150 C. In this pressure vessel brine and gas are allowed to equilibrate and then are drawn separately by pumps and injected in the core holder where the sample is confined under hydrostatic loading.

The pressure vessel has a thermocouple, pressure gauge and three separate ports to draw gas, brine and (gas+water) mixture.The core holder is capable of being operated at 3000 psi. The fluids exiting the core holder are received by the back pressure pump operated at a constant pressure receive mode of operation so that a constant back pressure is maintained. The back pressure pump is connected to the pre-saturation unit. The fluids received by the pump are delivered into the pre-saturation unit so that the pressure in the system is maintained and the fluids are recirculated in a closed loop. All the injection pumps (gas supply pump, gas injection pump, brine injection pump) are operated under constant flowrate injection mode. These pumps are capable of being operated up to a maximum pressure of 10,000 psi with the wetted parts of the pump made of Hastelloy – C. This steady state procedure was developed based on a similar flow system originally developed at the University of Wyoming (Piri, 2012)

The procedure for conducting single or multiphase flow experiments using the experimental set up shown in Figure 3.1 is described below.

1. Obtain a well preserved, fractured coal sample with diameter of 2" and length at least 4"
2. Prepare the sample by making sure the end faces are as flat as possible for complete mating with the flow distributors.
3. Mount the sample into the core holder.
4. Apply the required confining pressure.

5. Scan (X-ray CT) the entire length of the sample to obtain images of the sample in the dry state.
6. Vacuum saturate the sample using brine of known concentration.
7. Scan the entire length of the sample again to get images in the saturated state.
8. Start injecting brine from brine reservoir 1 at a pre-specified flow rate and monitor the pressure at the upstream and the downstream end of the sample. At the same time start the back pressure pump set at a constant pressure receive mode set at a specified value of pressure.
9. Record the pressure drop across of the sample after it has stabilized and change the flow rate to a new value and record the pressure drop after it has stabilized again.
10. Repeat the procedure by changing the flow rates for that particular confining pressure (the injection pressure must be monitored so as not to exceed the applied confining pressure).
11. Repeat the same procedure by applying different values of confining pressure and collecting a set of data points for the respective confining pressures.
12. After completion of this single phase injection test, allow the single phase injection to continue at some specified flow rate or preferably the first brine flow rate that is intended to be used in combination with the flow rate of gas for the two phase flow test.
13. Evacuate the pre-saturation pressure vessel so that air is removed from the system and brine is injected to about half to three quarters of the capacity of the vessel from reservoir 2. Next, gas is injected in to the vessel which already has water by using an injection pump connected to the supply gas cylinder. The initial pressure of the vessel is maintained below the value of the confining

pressure that is expected to be used and more or less in the neighborhood of the injection pressure that is currently observed from the previous step. The main purpose of the vessel is to equilibrate gas and water with each other.

14. Switch the brine supply so that brine is set to be drawn from the pre-saturation unit.
15. Start injecting gas at a pre-determined flow rate with the brine being continued to be injected at the set flow rate by the brine injection pump.
16. Observe the injection pressure profile. The injection pressures will continue to steadily increase.
17. Observe the pressure in the 'pre-saturation vessel' it will start to reduce when gas is being drawn by the gas injection pump
18. Using the gas supply pump inject some gas into the pre-saturation unit to maintain the pressure close to the prevailing injection pressure (this could be steadily increasing at this point).
19. The pressure in standby cylinder of the gas injection pump directly depends on the pressure in the pre –saturation vessel. If the pressure inside the standby cylinder is +/- 20 – 25 psi within the existing pressure at the inlet face of the sample, the standby cylinder will be able to increase/decrease pressure inside the standby cylinder so that the correct pressure is reached at the changeover. Therefore it is vital to maintain the pressure of the pre-saturation vessel close to the existing pressures at the inlet face of the sample.
20. This pressure maintenance of the pre-saturation unit does not affect the pressure of the brine phase inside the brine pump cylinders as it being an incompressible fluid, the standby cylinder will be able to reach the desired pressure irrespective of the current injection pressures.

21. If needed adjust the pressure setting of the back pressure pump, to minimize the oscillations
22. After a while, depending on the flow rates being used, the injection pressures and the back pressure will stabilize and record the upstream and downstream pressures
23. Scan the sample to get images of the sample at this saturation equilibrium corresponding to the ratio of brine and gas flow rate used
24. Now change the injection flow rates to the next new combination follow steps from 17 - 22
25. After completing the different gas and brine flow rate combinations and scanning them at the respective steady state conditions, stop the injection of brine and increase the flow rate of gas to the maximum flow rate possible.
26. After steady state conditions have been achieved with only gas flowing, the water in the core is in the irreducible and immobile saturation state. Scan the sample to get the images of the sample at this saturation condition.

After completing step 26 one set of effective/relative permeability curves has been obtained. To obtain a new set of curves at a different confining pressure, the entire procedure is repeated by at the new confining pressure.

It is to be noted that steps 1 to 12 outlines the procedure for conducting a single phase permeability test, while steps 13 to 26 describes the procedure for two phase flow tests. Figure 3.6 summarizes the whole procedure in a six step process.

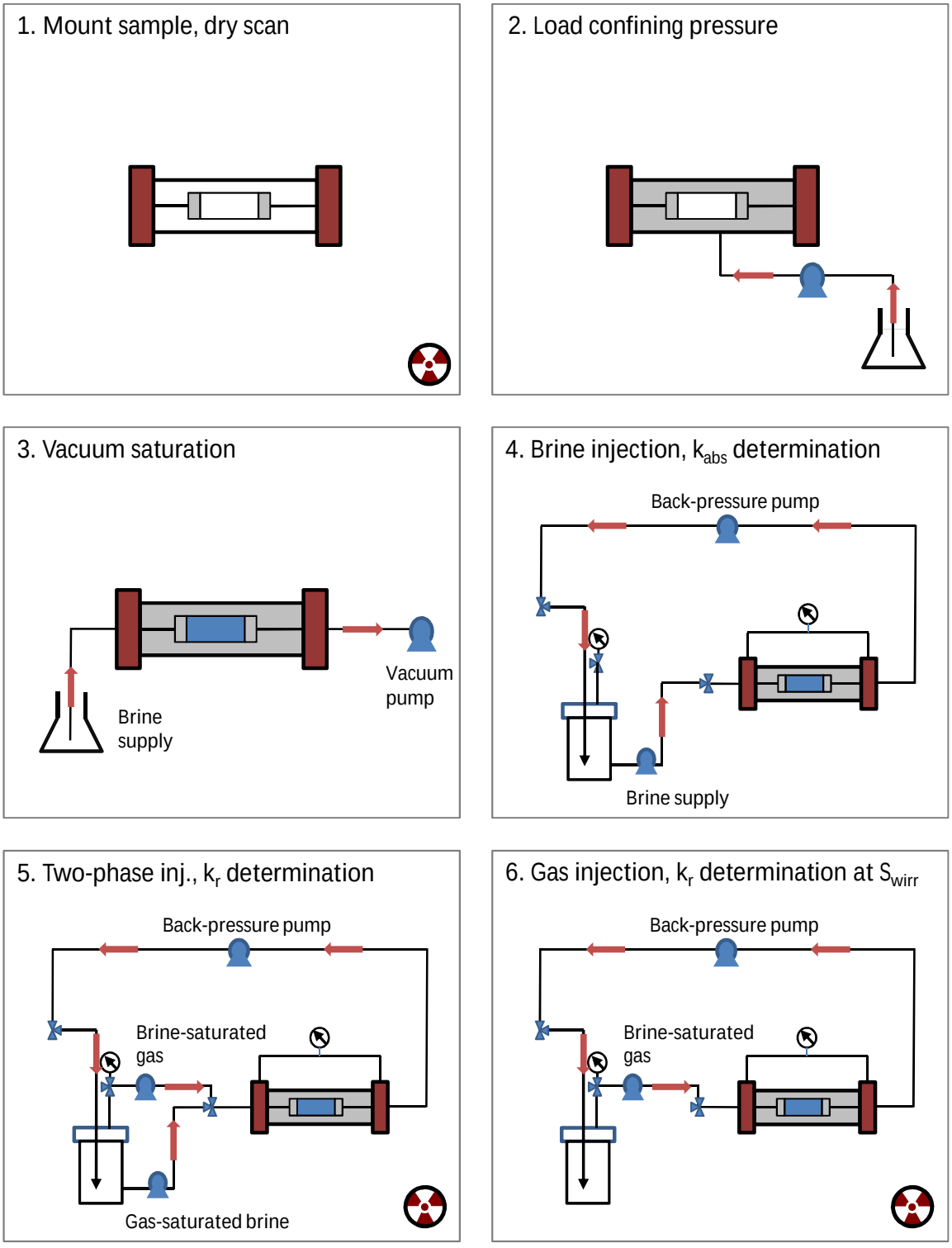

Figure 3-6. Flowchart outlining summary of the experimental procedure. Steps 5 and 6 are repeated for each confining pressure applied.

X-ray computed tomography

X–ray computed tomography is a non-invasive imaging technique used to visualize the internal structure of a material based on the specific attenuation of X rays by components of different densities present in it. The principle is that the object is viewed from multiple directions spanning over 360 degrees. Using these views, a two dimensional slice after each 360 degree rotation is reconstructed and stacked on top of each other to recreate the three dimensional view of the different componentsof the object (Denison et al., 1997).

The X-ray scanner used in this work is a 'Universal HD-350E' medical CT scanner, which has a series of detectors arranged on a circumference with the X-ray source rotating around the object positioned in the center. The resolution used here is 0.195mm × 0.195mm, with a slice thickness of 1mm and a detection frame of 512 × 512 voxels.

The primary objectives for scanning the coal samples used in this study are to visualize the internal structure of the sample to identify fracture network and connectivity, and to determine saturation of the flowing phases.

Absolute permeability measurements

Initial single-phase flow tests were conducted in sample 1 shown in Figure 3.7 to get a sense of the magnitude of the existing cleat permeability in the sample. Figure 3.7 shows the end faces of the sample and traversed fractures. Though it is possible to see some fracture network at the end faces of the core, the fracture connectivity and conductivity is uncertain. Distilled water

was used as the flowing phase for determining the absolute fracture permeability. Steps 1 through 4 described in Figure 3.6 were followed.

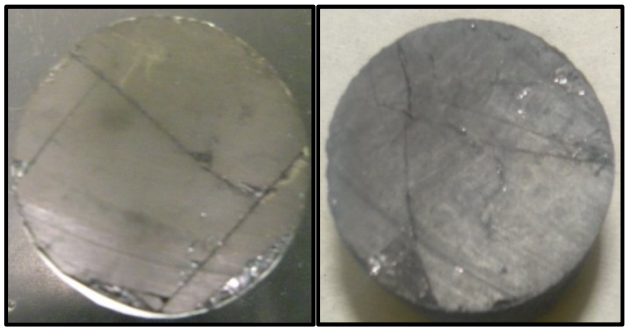

Figure 3-7. The end faces of sample 1 (D: 2", L: 2.8")

Figure 3.8 shows the flow velocity as a function of pressure drop per unit length of the sample in sample 1. Based on Darcy's law, a linear relationship exists between pressure drop and velocity and the slope of this line passing through the origin, gives the permeability of the sample. As seen in Figure 3.8, the relationship is clearly non-linear with very low velocities and high pressure drops. The permeability at each of these velocities is shown in Table 3.2.

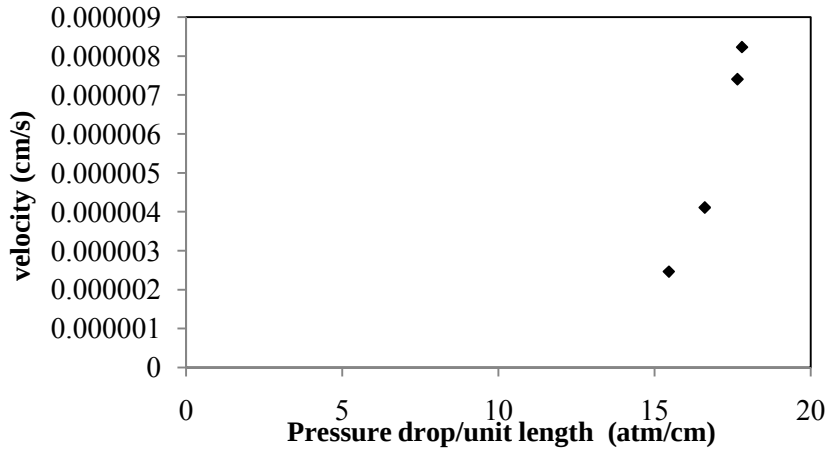

Figure 3-8. Flow velocity as a function of pressure drop per unit length – Sample 1

Table 3-2. Experimental observations for single phase permeability test – Sample 1 (Confining pressure = 2500 psi)

Flow rate (cc/s)	Fracture Permeability (mD)
1.0E-02	4.6E-04
9.0E-03	4.2E-04
5.0E-03	2.5E-04
3.0E-03	1.6E-04

This indicates that though there are some natural fractures present in the sample, the overall fracture permeability is low. This range of permeability is not generally considered to be well suited for laboratory determination of permeability of coal samples and generally samples having permeability > 0.1mD are considered suitable for flow experiments (Gash, 1991).

Sample stimulation and permeability experiments

Since sample 1 had very low absolute cleat permeability in the range of micro-darcies, a new sample was chosen (sample 2) and upon visual inspection it did not have any appreciable fractures. The sample was artificially fractured. The plot of velocity as a function of pressure drop experienced by the sample is shown in Figure 3.9. The relationship is linear and the average permeability was calculated to be around 7.4 mD.

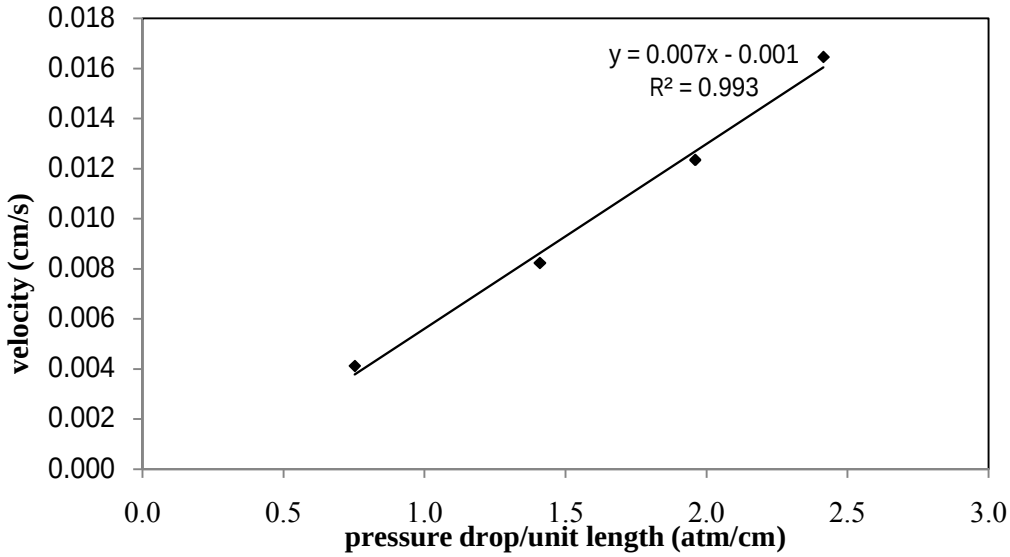

Figure 3-9. Flow velocity as a function of pressure drop per unit length - Sample 2

Sample 2 was X-ray CT scanned to map the internal structure of the sample. Figure 4.0 shows the images of the sample at different locations along the length of the sample. We can see the presence of fractures and their connectivity. The bright spots that we see in the image slices are the presence of minerals at different locations in the sample in the axial direction.

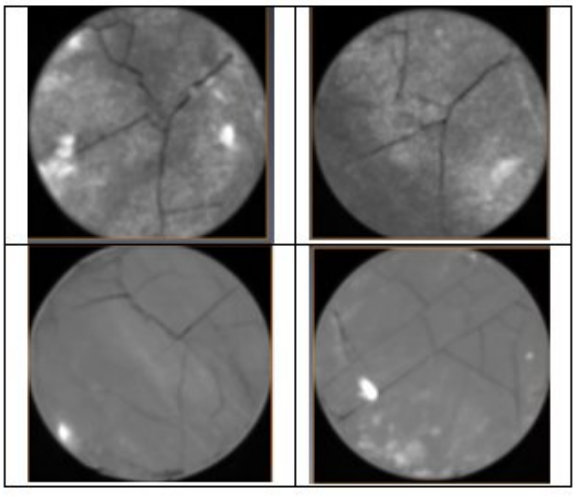

Figure 4-0. X–ray CT slices at four different locations in the axial direction - Sample 2

To determine the effect of effective stress on the absolute cleat permeability of the sample, the following different tests were conducted in the order shown below progressing with time.

Trial 1: Initial absolute fracture permeability determination by using water as the flowing phase

Trial 2: Absolute fracture permeability determination after the flow direction in the sample was reversed

Trial 3: Absolute fracture permeability determination after the flow direction in the sample was restored

Trial 4: Final determination of fracture permeability after the above three trials

The results and observations are discussed in chapter 4 under the section "Behavior of coal fracture permeability with changes in effective stress"

Relative permeability experiments with helium and brine

Multiphase flow tests were carried out in two different samples (Sample 3 & Sample 4) to understand the relative permeability characteristics when gas and water were flow at a predetermined ratio of flow rates.

Two-phase steady-state tests: Sample 3

Two sets of experiments were conducted with sample 3. One was done at a confining pressure of 300 psi and the other at 550 psi. The experiment was conducted based on the procedure described in section "Experimental setup and procedure"

Table 3.3 shows the flowrates of He and brine (5% w/w NaI solution) used, and the corresponding ratios at a constant confining pressure of 300 psi. Temperature during the experiment was 20±2 C. The last row highlighted in green correspond to the single phase, gas injection flow rate that was used to get the end point permeability of the gas phase at irreducible water saturation.

Table 3-3. Gas and liquid flow rates used for the multiphase flow test at $P_{confining}$ = 300 psi

q_{He}(cc/min)	q_{brine}(cc/min)	q_{br}/q_{He}
0.25	0.37	1.48
0.45	0.37	0.82
0.65	0.15	0.23
0.85	0.05	0.06
0.4	0.55	1.38
0.1	0.55	5.5
1.2	0.03	0.03
7	0	0

For each of the combination of flow rates shown in Table 3.3, sufficient time was allowed until steady state conditions were reached (pressure drop across the sample and the flow rates became constant) and the entire sample was scanned in the axial direction to record the saturation distributions of the gas and water in the fractures at that point in time. The effective permeability to gas and water were calculated using Darcy's law. The saturation of gas and water at a particular ratio of flow rates was calculated by using linear interpolation knowing the average CT number of the sample at dry and the 100% saturated state. The next test was done on sample 3 at a confining pressure of 550 psi. Table 3.4 shows the different combination of flow rates and the corresponding ratios used for this test. Again the last row in Table 3.4 represents the flow rate of

gas used for measuring the effective permeability to gas at irreducible water saturation. Before this test was conducted, the sample was relieved of confining pressure, dried, saturated and, the two-phase flow test was conducted again.

Table 3-4. Gas and liquid flow rates used for the multiphase flow test at $P_{confining}$ = 550 psi

q_{He}(cc/min)	q_{brine}(cc/min)	q_{br}/q_{He}
0.2	0.3	1.5
0.5	0.3	0.6
1	0.3	0.3
2	0.3	0.15
3	0.3	0.1
0.5	0.5	1
0.1	0.5	5
0.1	0.7	7
4	0.04	0.01
3	0	0

Two-phase steady-state tests: Sample 4

A similar two-phase flow experiment was repeated in sample 4 at confining pressures of 330 psi and 590 psi. Tables 3.5 and 3.6 show the flowrates and the corresponding flowrate ratios of water and gas at the two different confining pressures of 330 psi and 590 psi, respectively.

Table 3-5. Gas and liquid flow rates used for the multiphase flow test at $P_{confining}$ = 330 psi

q_{He}(cc/min)	q_{brine}(cc/min)	q_{br}/q_{He}
2	3	1.5
3.75	3	0.8
5	1	0.2
5	0.25	0.05
6	0.05	0.008
7	0.05	0.007
9	0.05	0.005
6	0	0

Table 3-6. Gas and liquid flow rates used for the multiphase flow test at $P_{confining}$ = 590 psi

q_{He}(cc/min)	q_{brine}(cc/min)	q_{br}/q_{He}
0.5	1.5	3
0.5	1	2
1.5	0.35	0.23
2.1	0.25	0.12
3.5	0.25	0.07
3.5	0.15	0.04
6	0	0

The bottom rows (highlighted in green) indicate the flow test that was conducted to measure the effective permeability to gas (He) at irreducible water saturation.

Relative permeability experiments with CO_2 and brine

Two-phase steady-state tests: Sample 4

To get a preliminary understanding of how the effective permeability of coal to gas and water changes by the introduction of CO_2 as the gas phase, CO_2-brine two-phase tests were initially conducted in sample 4. The same flow rate ratios shown in Tables 3.5 and 3.6 were used at a confining pressure of 330 psi and 590 psi. The experimental variables and conditions were maintained similar to that of the helium and brine two phase flow test conditions for comparison purposes.

Two-phase steady-state tests: Sample 5

Another new sample (sample #5) was used for conducting two-phase flow tests first with He-brine and followed by CO_2- brine. This sample was cored out using a water jet cutter from a coal block obtained from a nearby coal processing plant in Clearfield, PA. Tables 3.7 and 3.8 shows the combination of flowrates used in the two phase tests.

Table 3-7. Gas and liquid flow rates used for the multiphase flow test at $P_{confining}$ = 330 psi – Sample 5

q_{He}(cc/min)	q_{brine}(cc/min)	q_{br}/q_{He}	q_{CO2}(cc/min)	q_{brine}(cc/min)	q_{br}/q_{CO2}
0.17	0.5	2.94	0.17	0.5	2.94
0.17	0.25	1.47	0.17	0.25	1.47
2	1	0.5	2	1	0.50
2.5	1.2	0.48	2	0.96	0.48
3	0.5	0.17	3	0.5	0.17
4	0.1	0.03	4	0.1	0.03
5	0.05	0.01	5	0.05	0.01
6	0	0	6	0	0.00

Table 3-8. Gas and liquid flow rates used for the multiphase flow test at $P_{confining}$ = 590 psi – Sample 5

q_{He}(cc/min)	q_{brine}(cc/min)	q_{br}/q_{He}	q_{CO2}(cc/min)	q_{brine}(cc/min)	q_{br}/q_{CO2}
0.33	1	3.03	0.17	0.5	2.94
2.4	1.05	0.44	1.1428	0.5	0.44
3	1	0.33	1.515	0.5	0.33
3	0.5	0.17	3	0.5	0.17
4	0.1	0.03	4	0.1	0.03
5	0.05	0.01	5	0.05	0.01
6	0	0.00	6	0	0.00

Contrary to the relative permeability measurements presented in the previous section "Relative permeability experiments with He and brine", these were not scanned using the X-ray CT imaging procedure for estimating the phase saturation distributions. The results of these CO_2-brine two phase tests are discussed in Chapter 4 under the section "Behavior of fracture effective permeability of coal to CO_2 and brine"

Chapter 4

ANALYSIS OF RESULTS

Behavior of coal fracture permeability with changes in effective stress

Figure 4.1 shows the behavior of fracture (cleat) permeability in sample 2 with changes in effective stress for the experimental trials listed in chapter 3 under section "Sample stimulation and permeability measurements"

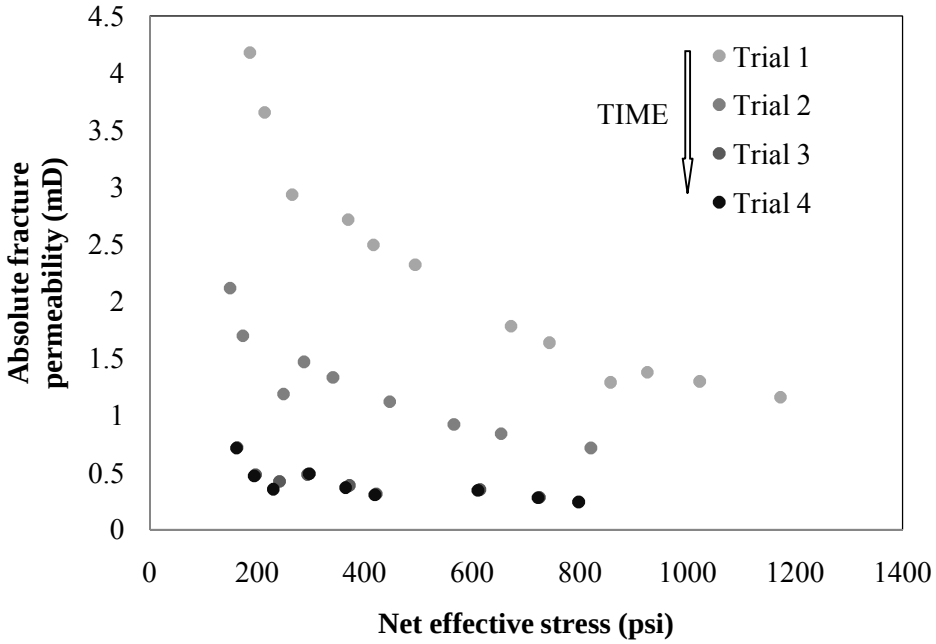

Figure 4-1. Variation of fracture permeability with net effective stress – Sample 2

One can see from Figure 4.1, the fracture permeability of the sample continuously decreases with time and after the fourth trial, the cleat permeability reduction is almost by an order magnitude lower from the initial cleat permeability. The entire duration of the tests starting from a fresh sample until the completion of the 4th trial is about 7 weeks. During these trials, the sample was subjected to alternating stress loading and unloading cycles and, with time and repetitive trials, the permeability keeps decreasing. This indicates that permeability continuously

decreases with repeated experimentation (single/multiphase flow tests) and it is difficult to restore to the original absolute permeability of the sample. Each time the core was stressed and de-stressed by the application/removal of confining pressure, the pore volume compressibility or the fracture compressibility was affected, and it subsequently changed the permeability of the sample irreversibly.

With continuous testing, the fracture compressibility becomes further reduced and it reaches a stage where the permeability is almost unaffected by the changes in effective stress (the fourth trial curve). Some other factors that could have affected the permeability measurement are the migration of fines which is difficult to control. The effective stress acting on the sample can lead to permanent structural changes by inducing a linear or a volumetric strain in the sample. These strains can alter the fracture volume compressibility which in-turn affects the permeability. The qualitative behavior of permeability decline with effective stress can be approximated to be exponential, although the behavior flattens out with time and could become independent of stress. Using an exponential permeability decline model for coal as shown in equation 4.1 (Seidle et al., 1992), the average fracture volume compressibility was estimated to be around 5E-4 psi^{-1}. Additionally, some hysteresis was also observed though not reported, when the absolute permeability of the sample was determined in the direction of increasing confining pressure and decreasing confining pressure.

$$k = k_i e^{-3Cf(\sigma_{eff})} \quad \text{----- (4.1)}$$

where,

k = fracture permeability (mD)

k_i = initial fracture permeability (mD)

c_f = fracture volume compressibility (1/psi)

σ_{eff} = effective stress (psi)

The behavior shown in Figure 4.1 is similar to the ones reported by Guo et al. (2008) when permeability of Canadian coal samples was calculated as a function of net stress by using non-adsorbing gas, and Shedid and Rahman (2009) when they used helium gas as the permeating fluid in Australian coal samples. It was concluded that the permeability of coal decreases with increase in effective stress and the permeability permanently changes to an irreversible value.

A similar observation was seen in sample 3 (Figure 4.2). Figure 4.2 shows two curves which represent the absolute permeability of the sample 3 as a function of effective stress.

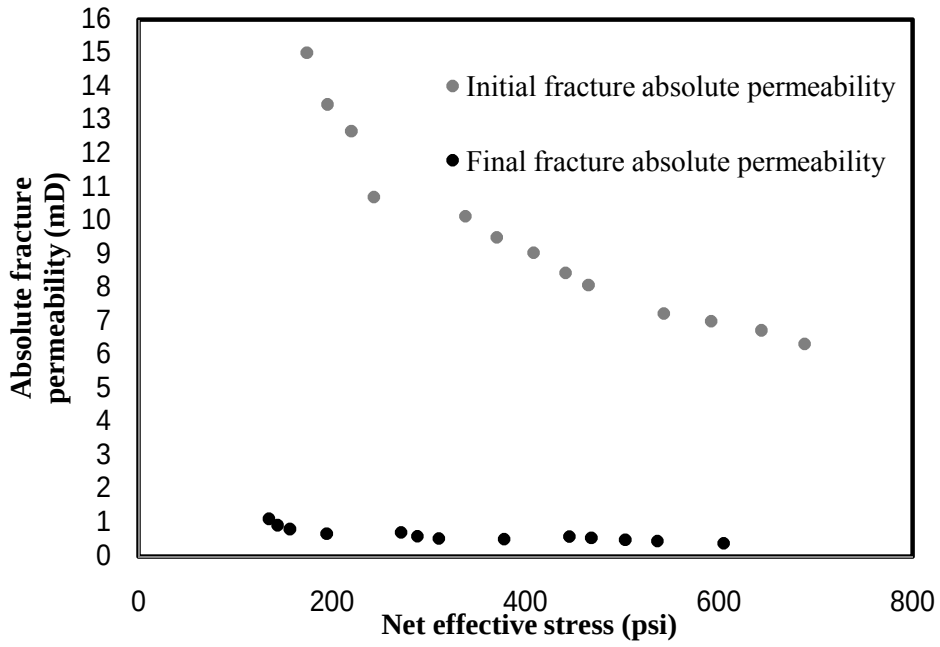

Figure 4-2. Fracture permeability of the sample before and after multiphase tests - Sample 3

The top curve represents the permeability variation as a function of effective stress before the two-phase test. The lower curve represents permeability of the sample after the two-phase test. As seen, the latest permeability of the sample is about one order less in magnitude in comparison to the initially observed permeability. Also the change in absolute permeability is

insignificant when compared to the initially obtained curve, and the permeability of the sample has declined with time and experimentation.

Behavior of fracture effective permeability with changes in confining pressure

Figure 4.3 and 4.4 show the effective permeability of gas and water in sample 3 (described in chapter 3) represented as a function of saturation of brine (S_w) at a confining pressure of 300 psi and 550 psi respectively.

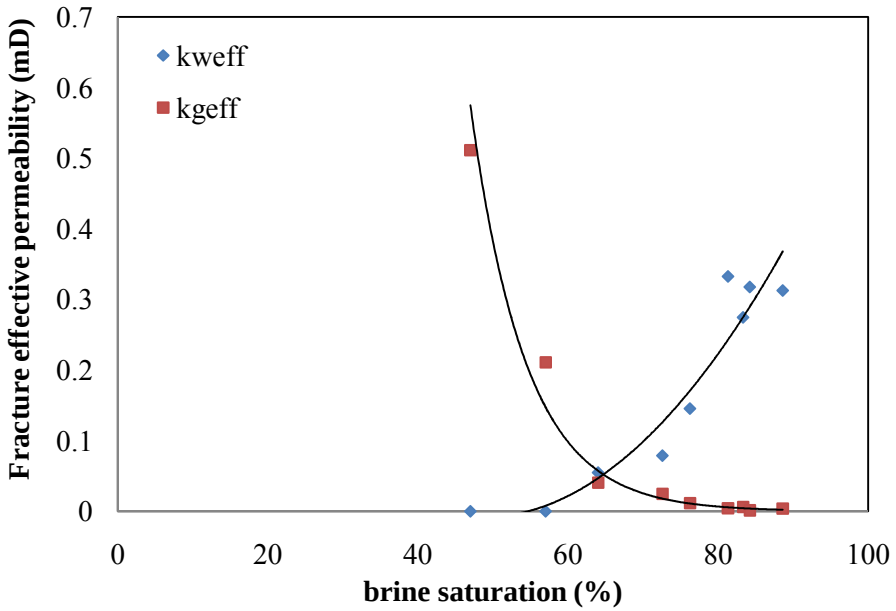

Figure 4-3. Fracture effective permeability of gas and water – Sample 3 (Pconf = 300 psi)

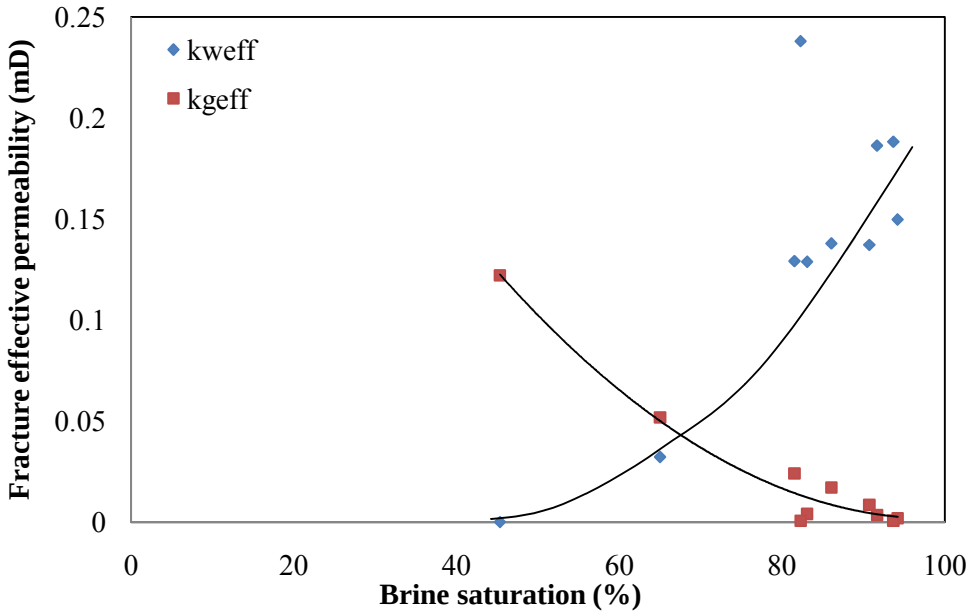

Figure 4-4. Fracture effective permeability of gas and water – Sample 3(Pconf = 550 psi)

In Figures 4.3 and 4.4 we can observe that the effective permeability to water is predominantly higher than the effective permeability to gas at the end points, irrespective of the confining pressures applied. The maximum effective permeability to gas at irreducible water saturation is 0.51 mD at a confining pressure of 300 psi, and 0.12 mD at a confining pressure of 500 psi. The corresponding irreducible water saturations are 45 % and 47% respectively.

The effective permeabilities of gas and water at the two different confining pressures used for sample 3 and sample 4 are plotted in the same plot in Figures 4.5 and 4.6, respectively. As the confining pressure is increased the magnitude of effective permeability to gas and water decreases. The relative change in the magnitude of the effective permeabilities for both water and gas from the lower confining pressure to the higher confining pressure is within an order of magnitude. The relative change is more pronounced for water in comparison to gas which is due to water being the continuous phase and it is impeding the flow of gas. This can be seen in Figures 4.5 and 4.6 by comparing the $k_{weff's}$ and the $k_{geff's}$. The magnitude of the effective

permeabilities of both water and gas are considerably lower in comparison to the initial absolute permeability of sample 3 which is shown in Figure 4.2 (ranges from about 15mD to 7 mD). From these observations in this type of coal, during the simultaneous flow of gas and water in the fracture network, the movement of gas is greatly affected in the presence of mobile water.

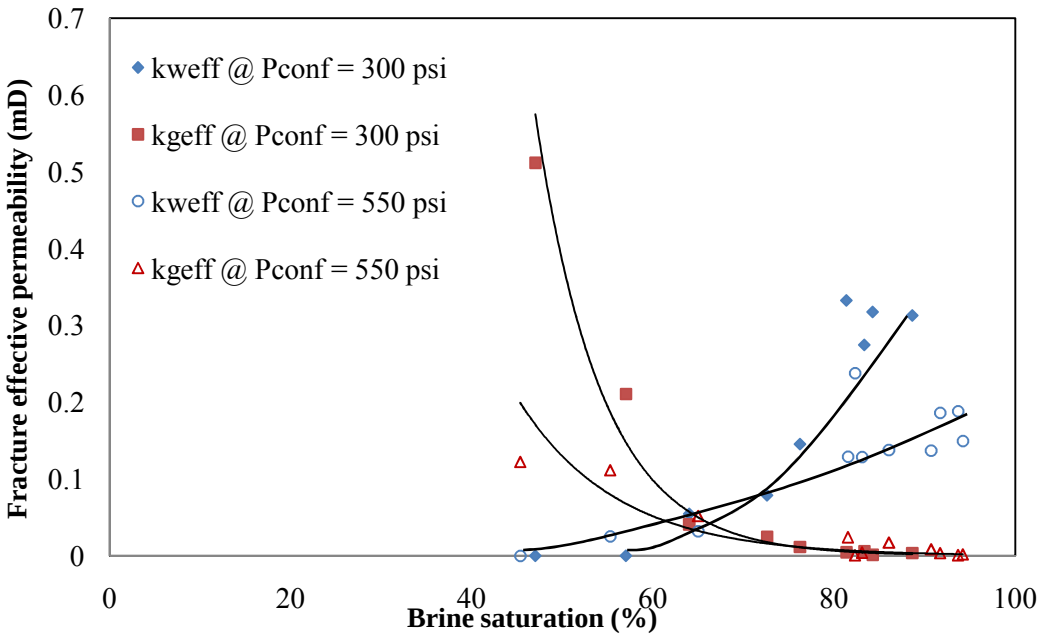

Figure 4-5. Fracture effective permeability of gas and water at different confining pressures – Sample 3

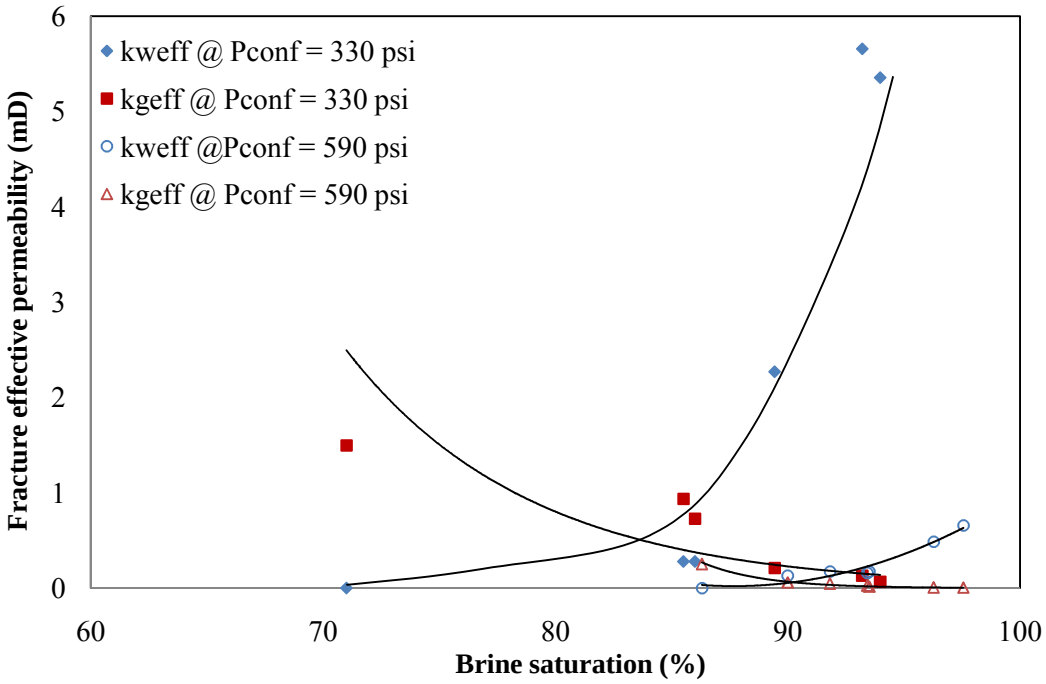

Figure 4-6. Fracture effective permeability of gas and water at different confining pressures – Sample 4

Persoff & Pruess (1995) conclude that the interference between gas and liquid during flow through a fracture having rough walls is very predominant and the relative permeabilities of the flowing phases are greatly reduced. Since coal is a fractured system, the fractures in this sample could have rough surfaces and the interference of the phases in the presence of each other drives the relative permeabilities down. Also, the inherent fracture geometry and connectivity as seen from the CT image in Figure 4.7 could contribute to the tortuous flow paths that gas and water have to take to travel through the fracture network, thus reducing the relative flow of the phases.

The effective permeability of a phase (gas or water) is higher when their saturations are higher, especially near the end points. Also, the effective permeability curves are shifted to the right hand side of the plot in the high water saturation region.

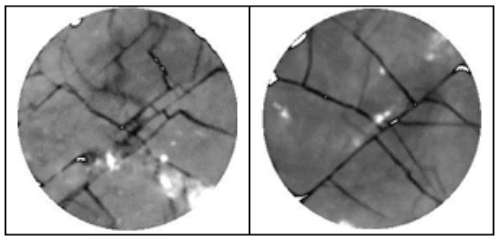

Figure 4-7. Fracture network in different slices – sample 4

Lian et al. (2012) report that in fractured carbonate formations, the stress sensitivity on permeability and relative permeability is significant. One of their conclusions is that the irreducible water saturation (S_{wirr}) increases and effective permeabilities, width of two-phase region and the cross-over point is lowered as the confining pressure increases. Similar observations can be made with respect to coal from Figures 4.8 and 4.9. This observation implies that fluid mobility is restricted to relatively high brine saturation.

In Figures 4.5 and 4.6 the cross over points decreases as the confining pressure increases in both the samples. This can be seen when comparing Figures 4.8 and 4.9.

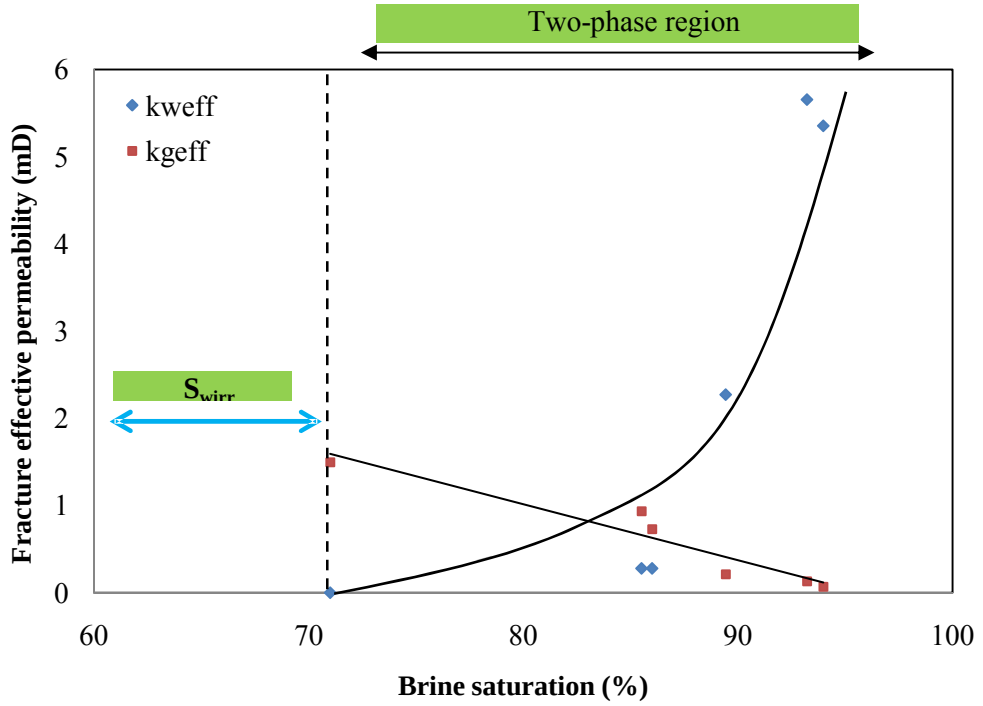

Figure 4-8. Fracture effective permeability of gas and water – Sample 4(Pconf = 330 psi)

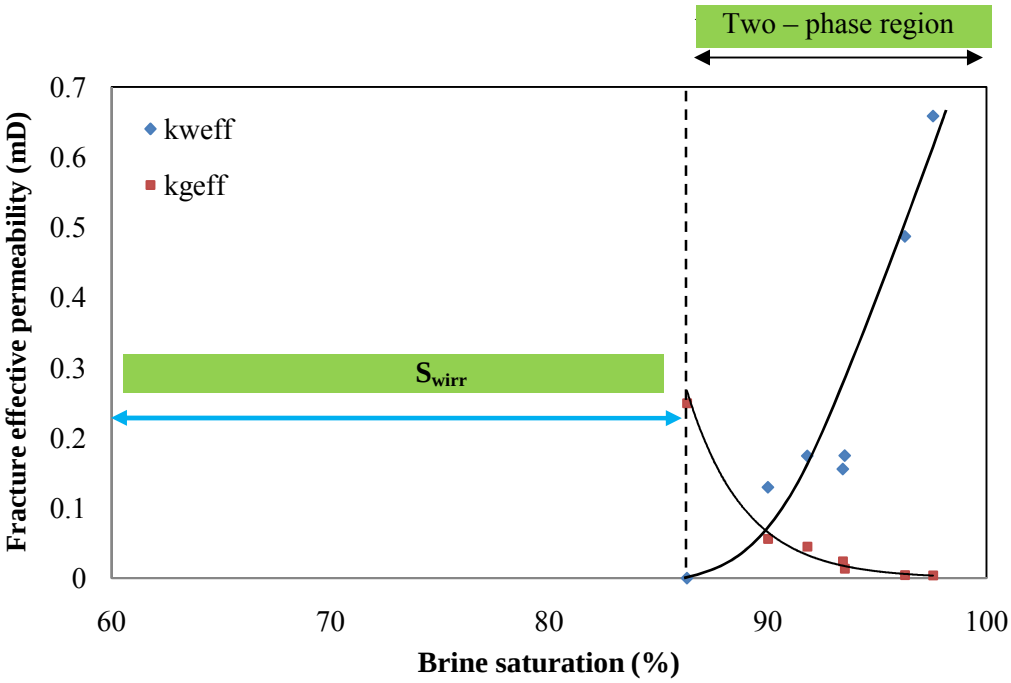

Figure 4-9. Fracture effective permeability of gas and water – Sample 4(Pconf = 590 psi)

The mobile two-phase flow region reduces when Figures 4.8 and 4.9 are compared as indicated by the horizontal double headed arrow (black). In Figures 4.3 and 4.4, the mobile two-phase region more or less remains the same. The immobile water saturation increases when the confining pressure increases, indicated by the horizontal double headed blue arrow in Figures 4.8 and 4.9. Due to greater confining pressure, the movement of water is reduced and it is retained in the cleats, resulting in higher immobile water saturation. Also the cleat network geometry could be influencing high water retention at higher confining pressures.

Behavior of fracture relative permeability with changes in confining pressure

Since absolute permeability changes with continued application of stress and also with time, the effective and relative permeability of the coal sample under consideration are dynamic entities too. Throughout the life of the coal bed methane reservoir, the absolute permeability will be changing due to the interplay of injection/depletion of fluids coupled with sorption characteristics of coal.

The relative fracture permeability curves shown in Figure 5.0 for sample 3 were obtained by dividing the effective fracture permeabilities (obtained at a confining pressure of 300 psi (Figure 4.3) by the absolute fracture permeabilites obtained using the top and the bottom curve from Figure 4.2 at the same value of effective stress at which the effective permeabilities were calculated. From Figure 5 we can see that the k_{rg} and k_{rw} obtained using the final absolute curves are higher in comparison to the relative fracture permeabilities obtained using the initial curve because of the magnitude of the kabs that divides the $k_{eff's}$. This does not imply that the relative fracture permeabilities of the phases will be higher if the total permeability of the cleat system is low, as we have seen earlier that with increase in confining pressure the absolute permeability decreases, and the effective permeability decreases to different extents implying that

the relative permeabilities should also decrease. In reality there must have been two sets of effective permeability curves one corresponding to the initial condition and other one corresponding to the final k_{abs} to compare the $k_{r's}$. Obtaining these two sets of effective permeabilities is difficult as the k_{abs} is continuously changing and the k_{eff}'s obtained in the experiment using sample 3 lies somewhere between the upper and the lower k_{abs} curves.

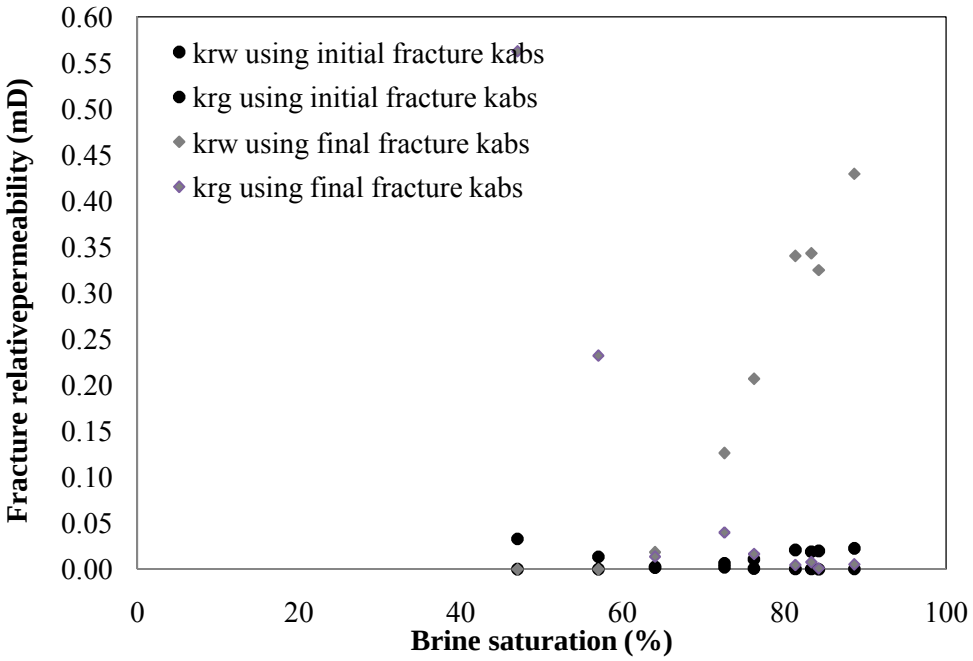

Figure 5-0. Fracture relative permeabilities ($P_{confining}$ = 300 psi)

- Sample 3

Behavior of fracture effective permeability with changes in effective stress

Figure 5.1 and 5.2 shows the variation of effective fracture permeability to water (k_{weff}) and the effective fracture permeability to gas (k_{geff}) with saturation and effective stress for sample 3.

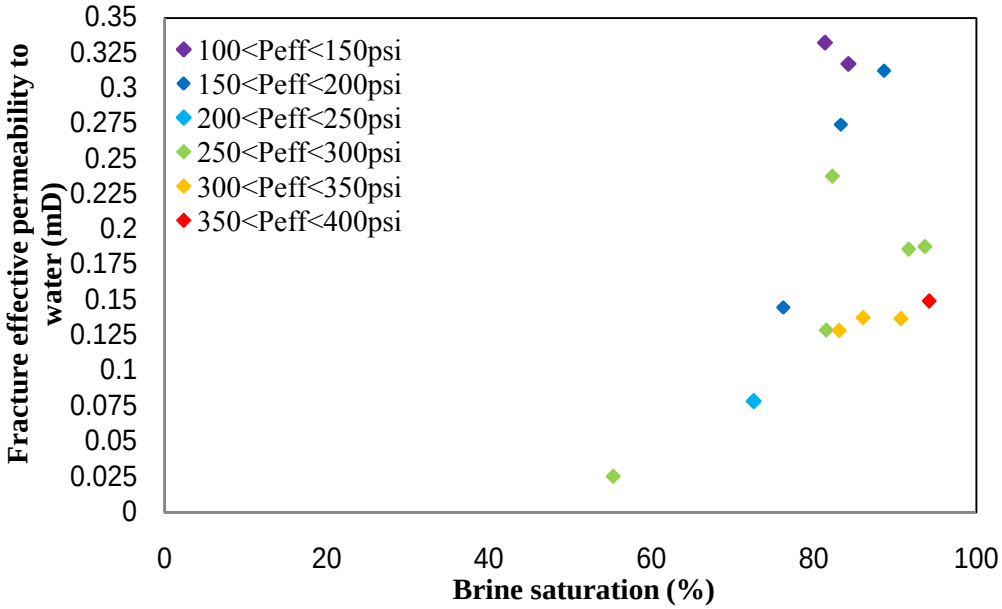

Figure 5-1. Fracture effective permeability to water as a function of effective stress and saturation – Sample 3

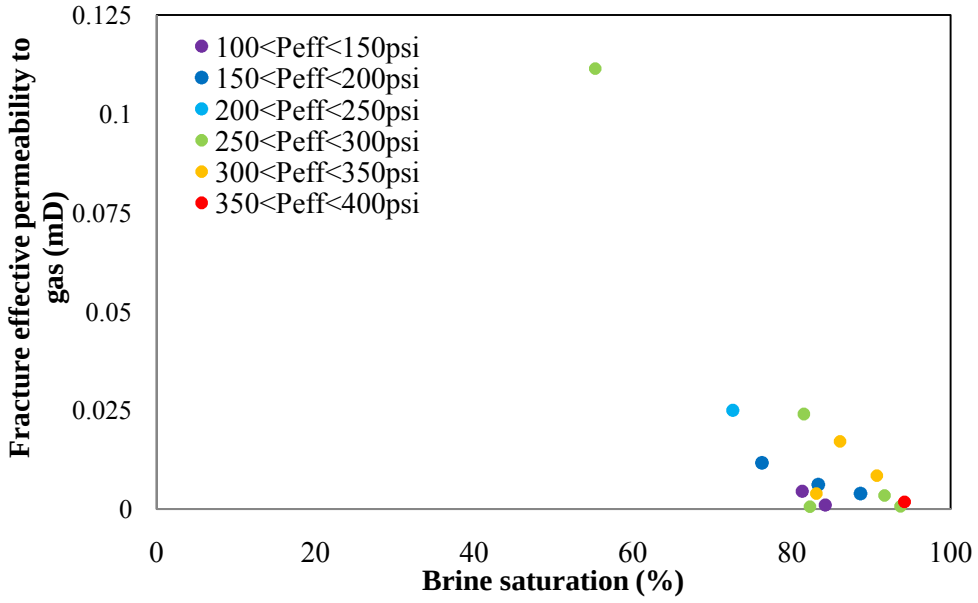

Figure 5-2. Fracture effective permeability to gas as a function of effective stress and saturation – Sample 3

Each of the data point is at a different effective stress and they are grouped together within a range of the effective stresses shown in the plot. The color coding to show the effective stress as the third parameter varies from a cooler color to a warmer color to show increasing levels of effective stress. In Figure 5.1 the k_{weff} decreases as the effective stress increases and for the lowest k_{weff} at highest effective stress the saturation is higher. In Figure 5.2 it is difficult to see a clear relationship between effective permeability to gas and saturation at a particular effective stress and what is clear is that effective permeability to water is more sensitive to changes in effective stress than effective permeability to gas. Figures 5.3 and 5.4 show similar plots but for sample 4. The k_{weff} decreases with the increase in effective stress and the decrease in the magnitude of k_{weff} is more explicitly seen due to a higher absolute permeability when compared to sample 3. Also in Figure 5.4, the variation of k_{geff} with effective stress is seen more clearly when compared to Figure 5.2. As the effective stress increases, the k_{geff} decreases and the lowest k_{geff} at the highest effective stress has the lowest gas saturation.

In Figures 5.3 and 5.4 each color contour corresponds with a single set of effective permeability for a particular effective stress range. This implies that there can exist a family of effective and relative permeability curves so that the effective permeability of coal to gas and water could be represented as a surface instead of a two dimensional relationship relating permeability and saturations alone.

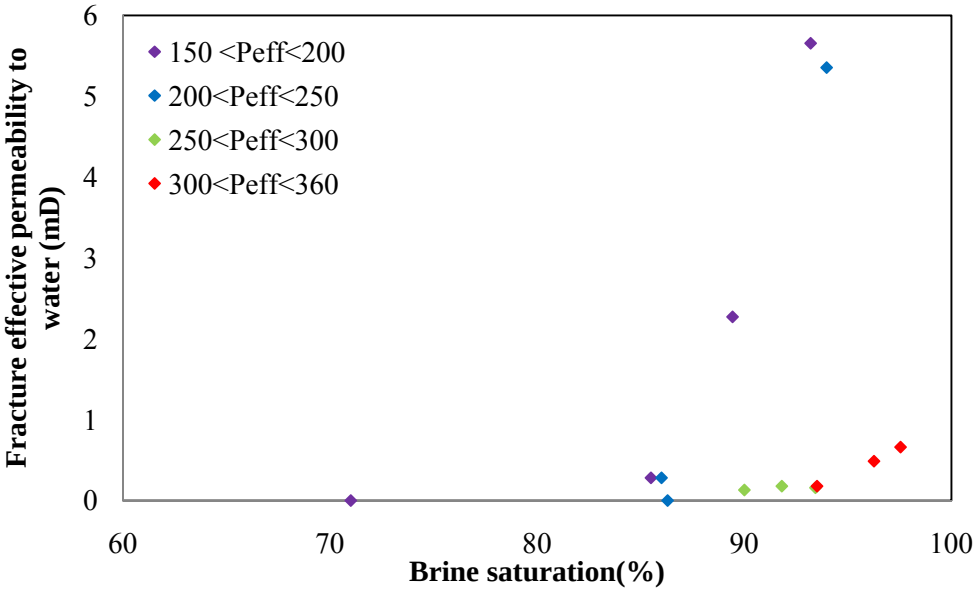

Figure 5-3. Fracture effective permeability of water as a function of effective stress and saturation – Sample 4

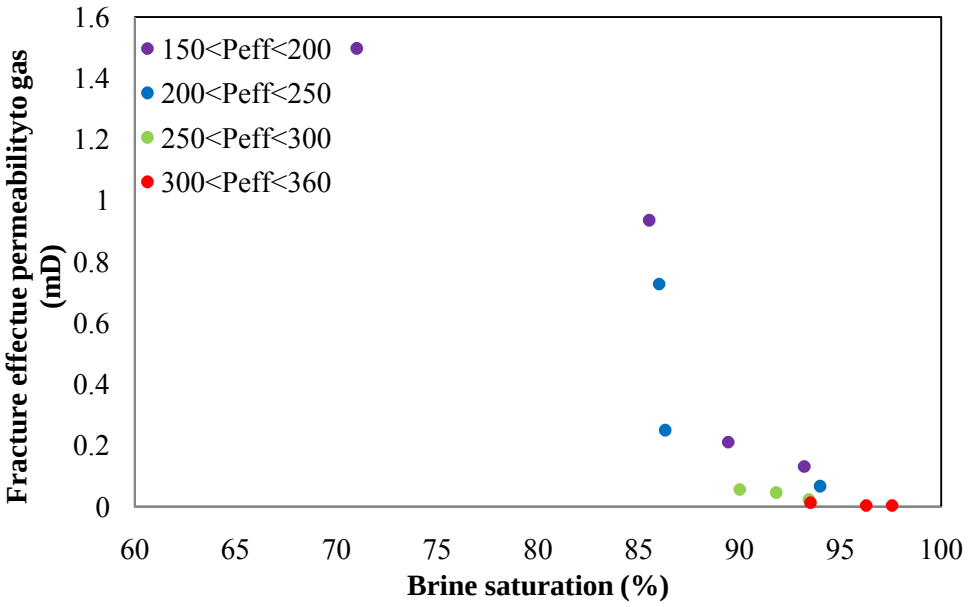

Figure 5-4. Fracture effective permeability of gas as a function of effective stress and saturation – Sample 4

Behavior of fracture effective permeability of coal to CO_2 and brine

Figures 5.5 and 5.6 show the effective fracture permeability of coal to water and gas obtained when using CO_2 and brine, as a function of the ratio of flowrate of brine to gas. In these figures, the CO_2-brine effective permeabilities are compared against the effective permeabilities of water and gas when helium and brine were used as the flowing phases. Figure 5.5 correspond to the test conducted at 330 psi confining pressure and figure 5.6 correspond to the test conducted using a confining pressure of 590 psi.

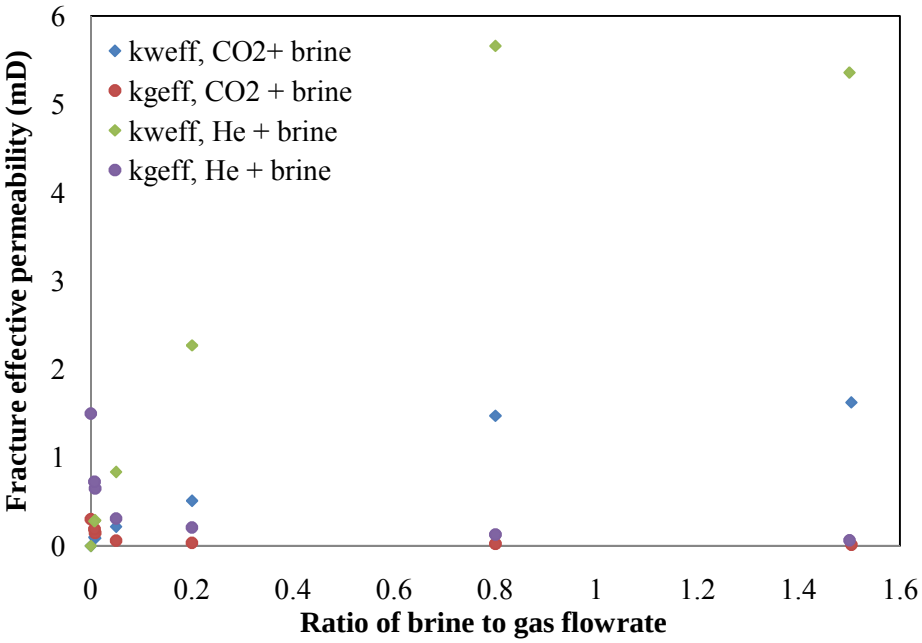

Figure 5-5. Fracture effective permeability to water and gas as a function of ratio of flowrates – Sample 4, Confining pressure: 330 psi

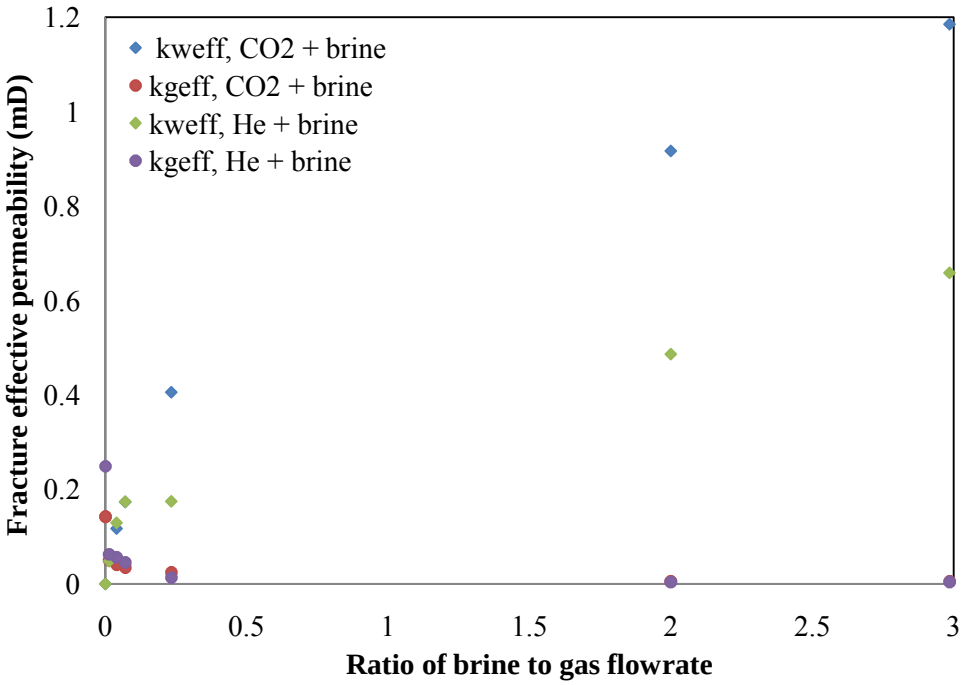

Figure 5-6. Fracture effective permeability to water and gas as a function of ratio of flowrates – Sample 4, Confining pressure: 590 psi

From figure 5.5, one can see that the fracture effective permeabilities of coal to both gas and water for the case of brine and CO_2 are lower in comparison to the effective permeabilities obtained using helium and brine for the same ratio of flowrates used. This could be due to the fact that CO_2 is adsorbing, thereby reducing the fracture effective permeabilities. However, this can also be due to the increase in effective stress that is causing the permeabilities to decrease. Table 4-1 shows the effective permeabilities of brine and gas listed as a function of effective stress and the ratio of flow rates used for the confining pressure of 330 psi.

Table 4-1. Fracture effective permeability of coal to water and gas: confining pressure: 330 psi – Sample 4

CO_2	**He**	**CO_2**	**He**	q_{brine}/q_{gas}	**He+ brine**	**CO_2 + brine**
k_{weff}(mD)	k_{weff}(mD)	k_{geff}(mD)	k_{geff}(mD)	(dimensionless)	P_{eff}(psi)	P_{eff}(psi)
1.62	5.36	0.02	0.07	1.5	207.5	127.5
1.47	5.66	0.03	0.13	0.8	192.5	119
0.51	2.27	0.04	0.21	0.2	197.5	144.5
0.22	0.84	0.06	0.31	0.05	207	164
0.09	0.29	0.15	0.65	0.01	212.5	160
0.1	0.28	0.19	0.73	0.01	206	154
0	0	0.3	1.5	0	186	166.5

From Table 4.1 by comparing the fracture effective permeability of coal to CO_2 and brine to the corresponding fracture effective permeabilities obtained using He -brine , one can observe that though the k_{weff} and k_{geff} obtained using CO_2 + brine is lower in comparison to the k_{weff} and k_{geff} obtained using He + brine , the corresponding effective stresses are lower. This can be seen by comparing columns 6 and column 7. This implies that the effective permeabilites have decreased as a result of interaction (adsorption) of CO_2 with the sample.

Figure 5.6 is similar to figure 5.5 but with data obtained at the higher confining pressure of 590 psi. From figure 5.6 , one can observe that the effective permeability of coal to gas and water (CO_2+ brine) is higher in comparison to corresponding effective permeabilities (He+brine). Table 4.2 shows the effective permeabilities of brine and gas listed as a function of effective stress and the ratio of flow rates used for the confining pressure of 590 psi. By looking at Table 4.2 we can also observe that the effective stresses obtained during the CO_2 + brine experiment is higher in comparison to the He + brine experiment .Therefore an anomalous behavior is observed here.

Table 4-2. Fracture effective permeability of coal to water and gas: confining pressure: 590 psi – Sample 4

CO_2	**He**	**CO_2**	**He**	q_{brine}/q_{gas}	**He**	**CO_2**
k_{weff}(mD)	k_{weff}(mD)	k_{geff}(mD)	k_{geff}(mD)	(dimensionless)	P_{eff}(psi)	P_{eff}(psi)
1.19	0.66	0.01	0.004	2.99	342.5	358
0.92	0.49	0.01	0.005	2	357.5	319
0.41	0.17	0.03	0.014	0.23	309	255
0.17	0.17	0.05	0.045	0.07	269	333.5
0.12	0.13	0.05	0.056	0.04	272.5	364
0.05	0.05	0.07	0.063	0.01	279	385.5
0	0	0.19	0.249	0	220	422.5

To validate the behavior of CO_2 and brine effective permeabilities at higher effective stresses, similar tests were conducted in a new sample (sample # 5). Figures 5.7 and 5.8 shows the effective permeabilities represented as a function of the ratio of flow rates when brine + He and brine + CO_2 were used as the flowing phases.

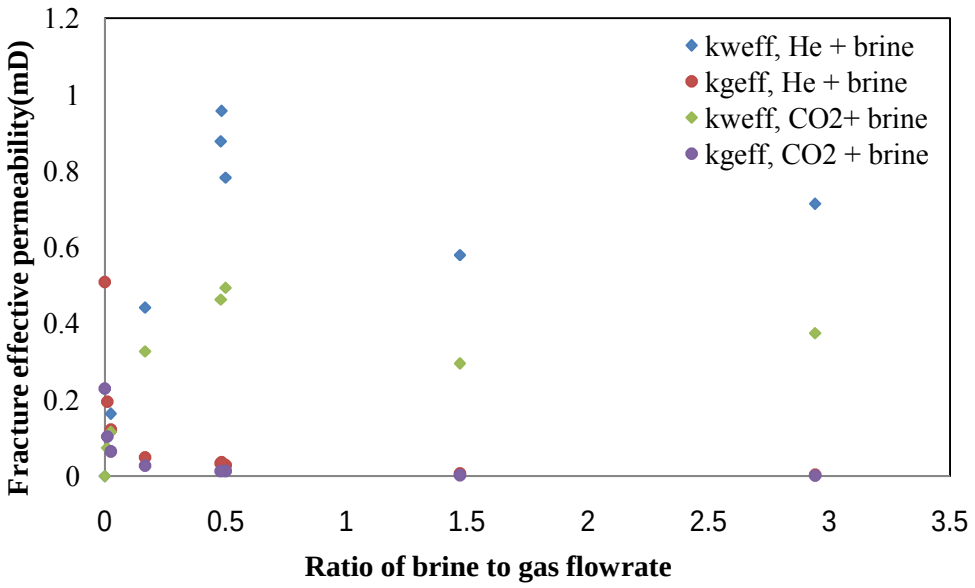

Figure 5-7. Fracture effective permeability of water and gas as a function of ratio of flowrates – Sample 5, Confining pressure: 330 psi

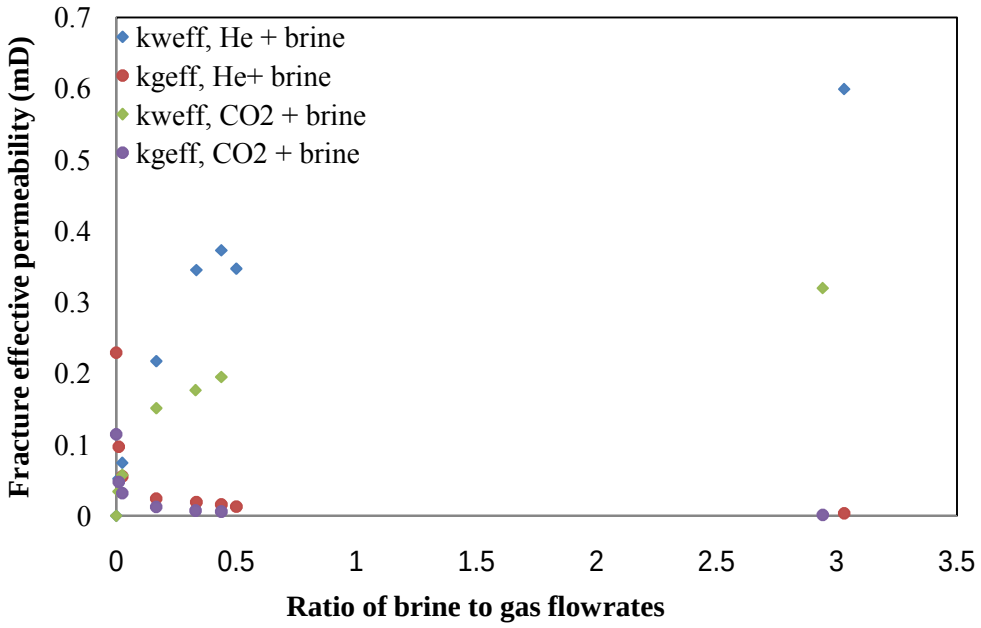

Figure 5-8. Fracture effective permeability of water and gas as a function of ratio of flowrates – Sample 5, Confining pressure: 590 psi

From figures 5.7 and 5.8 one can observe that the effective permeabilities to water and gas obtained from the CO_2 + brine test are lower in comparison to the effective permeabilities when Helium and brine were used as the flowing phases. This implies that there is a definite reduction in permeability of the phases when CO_2 is used. Tables 4.3 and 4.4 show effective permeabilities obtained from sample # 5 as a function of ratio of flow rates and effective stress acting on the sample.

Table 4-3. Fracture effective permeability of coal to water and gas: confining pressure: 330 psi – Sample 5

CO_2 kweff(mD)	**He** kweff(mD)	**CO_2** kgeff(mD)	**He** kgeff(mD)	**q_{brine}/q_{gas}** (dimensionless)	**He** Peff(psi)	**CO_2** Peff(psi)
0.37	0.71	0.002	0.005	2.94	217	198
0.3	0.58	0.003	0.007	1.47	233.5	228
0.49	0.78	0.014	0.029	0.5	178.5	155.5
0.46	0.88	0.013	0.034	0.48	156	147.5
0.33	0.44	0.027	0.049	0.17	182.5	163
0.12	0.16	0.065	0.122	0.03	217.5	187
0.07	0.11	0.104	0.196	0.01	220.75	197.5
0	0	0.229	0.509	0	225.5	87.5

Table 4-4. Fracture effective permeability of coal to water and gas: confining pressure: 590 psi – Sample 5

CO_2 kweff(mD)	**He** kweff(mD)	**CO_2** kgeff(mD)	**He** kgeff(mD)	**q_{brine}/q_{gas}** (dimensionless)	**He** Peff(psi)	**CO_2** Peff(psi)
0.32	0.6	0.002	0.004	3.03	436.5	434
0.2	0.37	0.006	0.016	0.44	277	362.5
0.18	0.35	0.007	0.019	0.33	272	316
0.15	0.22	0.013	0.024	0.17	318.5	252
0.06	0.07	0.032	0.055	0.03	378.5	283
0.03	0.05	0.048	0.097	0.01	383	300
0	0	0.115	0.229	0	380	345

From Table 4.3, we can observe that for the case of the tests conducted at 330 psi confining pressure, the effective permeabilities are lower for the case when CO_2+ brine was used. The corresponding effective stresses are lower implying that though the effective permeabilities are lower when CO_2 is used, the decrease in effective permeability is due to the adsorption of CO_2 on the coal surface. This observation is similar to the one seen in Table 4.1. From Table 4.4, a similar observation can be noted, that is, the effective permeability of coal to gas and water decreases when CO_2 is used as the gas phase but these effective permeabilities are recorded at lower effective stresses with the exception of two data points highlighted in gray. This trial in sample 5 confirms that even at higher effective stresses, the swelling effect caused by CO_2 is present. The other observation to be identified is whether this reduction in permeabilities is due to a change in effective stress as result of CO_2 adsorption on coal surfaces or due to the changes in effective stress due to increase in pore pressure. Figures 5.9 and 6.0 show the effective permeability of coal to CO_2 plotted as a function of effective stress at a confining

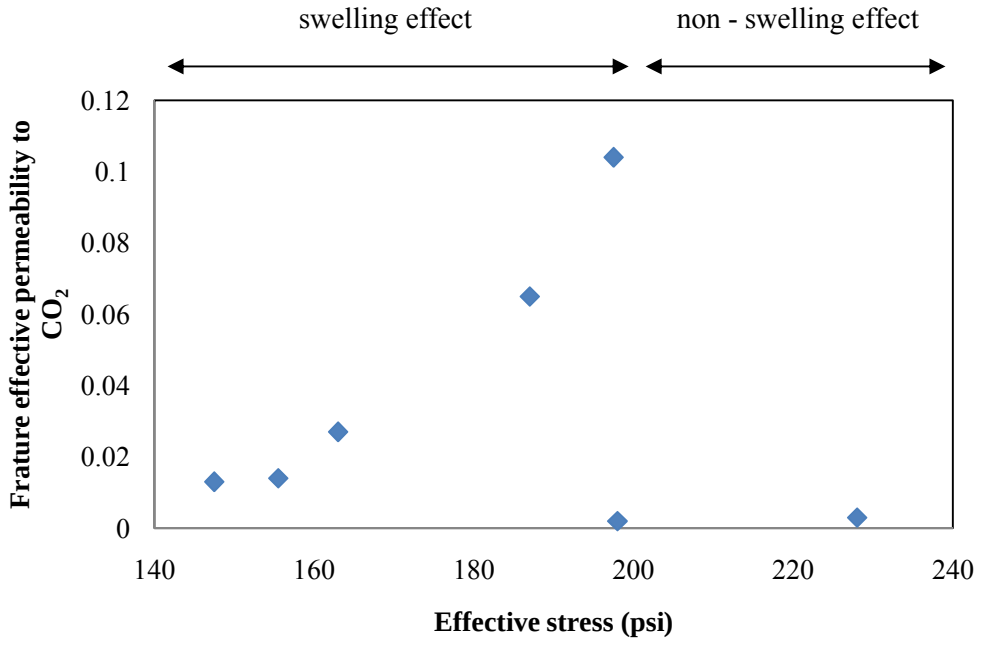

Figure 5-9. Fracture effective permeability of coal to CO_2 as a function of effective stress – Sample 5, Confining pressure: 330 psi

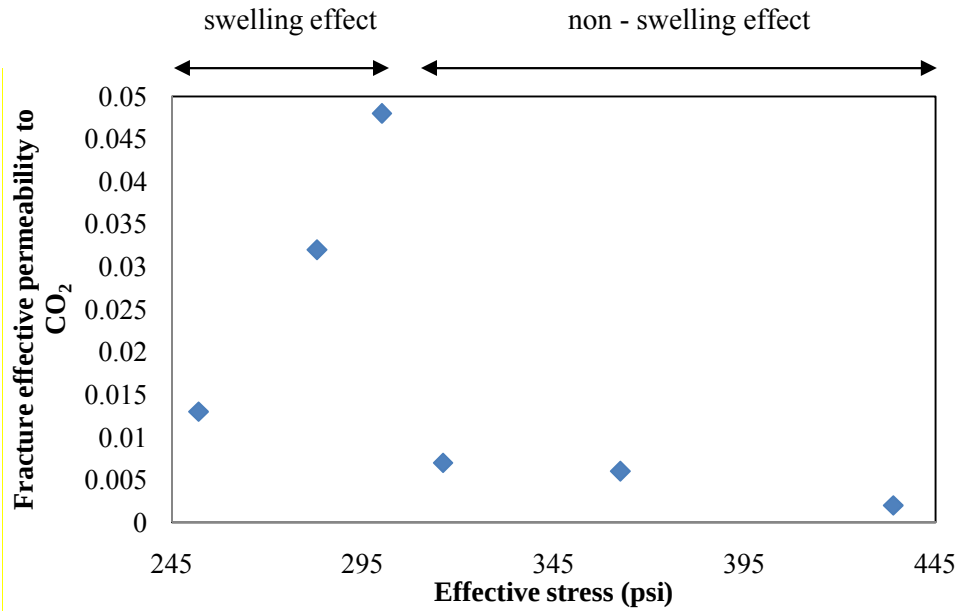

Figure 6-0. Fracture effective permeability of coal to CO_2 as a function of effective stress – Sample 5, Confining pressure: 590 psi

pressure of 330 psi and 590 psi respectively. Based on figures 5.9 and 6 one can observe that as the effective stress decreases the permeability increases and after a certain point, the permeability starts to decline indicating the effect of swelling dominates resulting in subsequent permeability reduction.

By conducting CO_2-brine flow experiments one was able to see the effective transport of fluids in the fractures is more restricted in comparison to the He-brine flow experiments. The fracture effective permeability of coal to gas and water is lower in the case of CO_2-brine flow experiments. This indicates that using representative relative permeability relationships would be more suitable to describe the simultaneous transport of gas and liquid during the primary or enhanced recovery of methane from coal seams.

Surface representation of fracture effective permeabilities

Figure 6.1 shows the same information depicted in figure 5.3. The additional information in figure 5.9 is that the two vertical double headed arrows that show the boundaries of saturation between 71 % and 94 % and a double headed dotted black arrow. Here one can see that for any value of saturation there can be more than one value of effective permeability as shown by the black dotted line, depending on the effective stress. The reason for choosing these two end points with respect to saturation is that the lower boundary represents the S_{wirr} and the higher boundary represents the saturation upto which there can be multiple effective permeabilities.

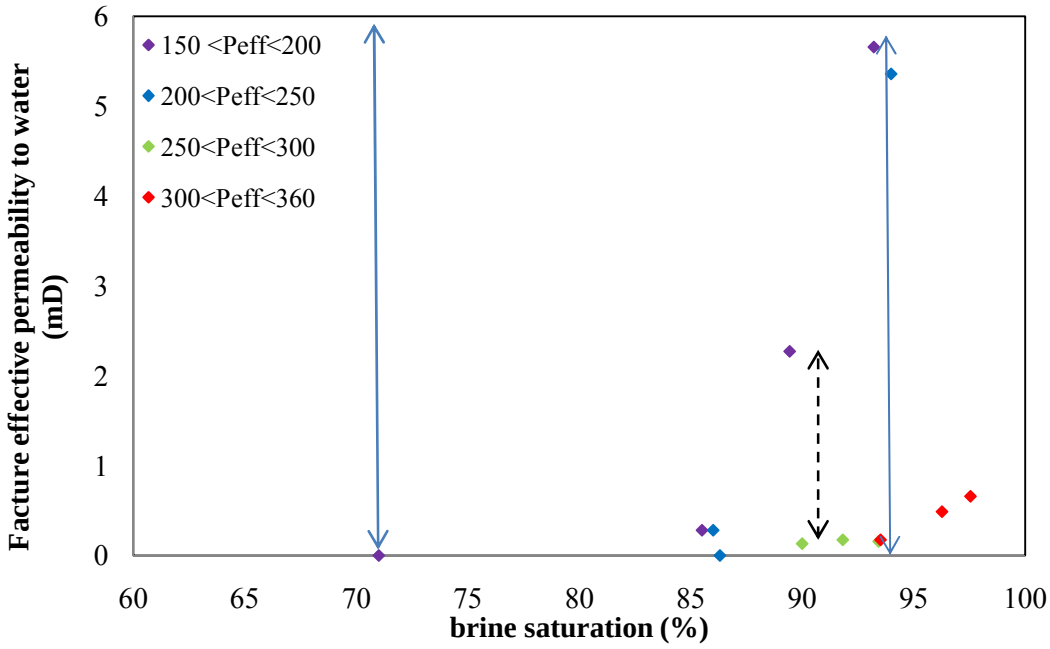

Figure 6-1. Effective permeability of water as a function of effective stress and saturation – Sample 4: Illustration to show multiple effective permeabilities

Hence to construct a fracture effective permeability surface as a function of effective stress and saturation, first a two dimensional curve fit is done to fit the individual sets of the

effective permeability curves obtained for the range of effective stress. Next a complete set of effective permeability values are generated based on this two dimensional fit, between the prescribed saturation boundaries. Once we have the generalized effective permeability curves, then a three dimensional plot is constructed that displays effective permeabilities as a function of saturation and the corresponding effective stresses. To illustrate this procedure, the equation given below was obtained after fitting the saturation and effective permeabiltites corresponding to data obtained for effective stresses in between 150 and 200 psi in Figure 6.1

$$k_{weff} = 4.34e\text{-}11 * \exp(0.2747 * S_w)$$

Using the above equation, the values of k_{weff} corresponding to the saturation values ranging between 71% and 90% were calculated. In a similar way, respective effective permeability equations were generated for the different effective stress ranges. Now using the generated values of $k_{weff's}$ for different effective stress's and saturations , the best fit surface showing the variation of $k_{weff's}$ with the other two variables was generated are shown in figure 6.2.

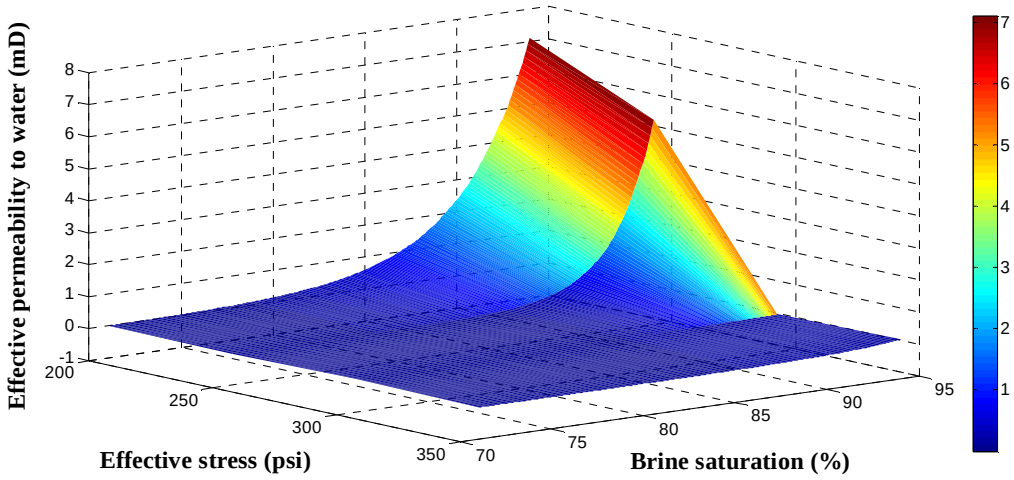

Figure 6-2. Fracture effective permeability to water: surface representation – Sample 4

For the same sample 4, a similar surface plot can be generated for the fracture effective permeability of coal to gas as shown in figure 6.3

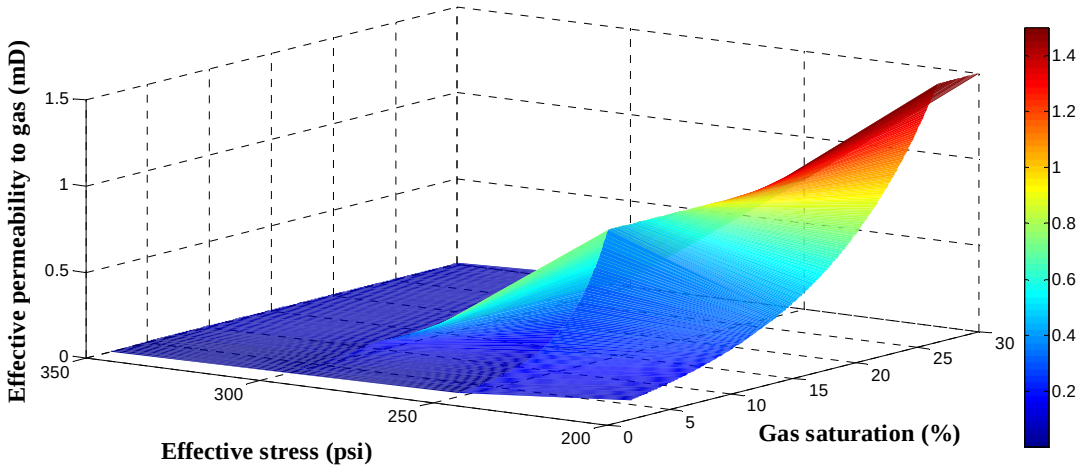

Figure 6-3. Fracture effective permeability to gas: surface representation – Sample 4

From the above two surfaces shown, an equation of the surface can be generated which relates the effective permeability as a function of effective stress and fluid saturation. This relationship can be used in reservoir models using an appropriate formulation to relate the relative permeability changes as a function of net stress and saturation.

Chapter 5

RESERVOIR SIMULATION STUDIES FOR CBM PRODUCTION ANALYSIS

Reservoir simulators serve as one of the vital tools available to better understand the dynamics of fluid recoveries at the field scale based on experimental or field derived data as inputs. To test the impact of the experimentally obtained relative permeability relationships at different effective stress conditions, several scenarios were conducted to determine its impact on the primary recovery. In this work, an in-house finite difference based compositional coal bed methane simulator, PSU – COALCOMP (Manik et al., 2000; Thararoop et. al., 2009; Aslan , 2013) and a commercial compositional CBM simulator, CMG-GEM developed by Computer Modeling Group (Calgary, Canada) were used for the numerical study. Some of the features of the numerical models are given below.

- Dual permeability, dual porosity formulation
- Multi-mechanistic fluid transport modeling
- Multi-component sorption modeling
- Horizontal and vertical wells modeling
- Bottom-hole pressure and flowrate specification functionalities

Table 4-5 shows the description of the different scenarios.

Table 4-5. Description of the different modeling cases

Case 1	Primary CBM recovery with X- type kr curves
Case 2	Primary CBM recovery with relative permeability curves used in commercial simulators (Law et al., 2002)
Case 3	Primary CBM recovery with experimental k_r's – set 1
Case 4	Primary CBM recovery with experimental k_r's – set 2
Case 5	Primary CBM recovery with experimental k_r's – set 3
Case 6	Primary CBM recovery with multiple relative permeability relationships based on effective stress regimes

Table 4.6, 4.7, 4.8 & 4.9 show the different relative permeability relationships used for evaluating the different cases described in Table 4.5

Table 4-6. Relative permeability curves used in commercial CBM simulators (Law et al., 2002)

Water saturation	Relative permeability to water	Relative permeability to gas
1	1	0
0.975	0.814	0.0035
0.95	0.731	0.007
0.9	0.601	0.018
0.85	0.49	0.033
0.8	0.392	0.051
0.75	0.312	0.07
0.7	0.251	0.09
0.65	0.2	0.118
0.6	0.154	0.147
0.55	0.116	0.18
0.5	0.088	0.216
0.45	0.067	0.253
0.4	0.049	0.295
0.35	0.035	0.342
0.3	0.024	0.401
0.25	0.015	0.466
0.2	0.007	0.537
0.15	0.002	0.627
0.1	0.0013	0.72
0.05	0.0006	0.835
0	0	1

Table 4-7. Relative permeability – Experimentally determined: set 1

Water saturation	Relative permeability to water	Relative permeability to gas
0	0	0.75
0.71	0	0.75
0.89	0.76	0.11
0.93	1	0.07
1	1	0

Table 4-8. Relative permeability – Experimentally determined: set 2

Water saturation	Relative permeability to water	Relative permeability to gas
0	0	0.11
0.86	0.04	0.11
0.9	0.2	0.03
0.94	0.9	0.01
1	0.9	0

Table 4-9. Relative permeability – Experimentally determined: set 3

Water saturation	Relative permeability to water	Relative permeability to gas
0	0	0.02
0.88	0.01	0.02
0.9	0.02	0.009
0.92	0.03	0.008
1	0.03	0

The relative permeability descriptions shown in Tables 4.7, 4.8 and 4.9 were derived from the effective permeabilities shown in Figures 5.3 and 5.4 at the corresponding effective stress ranges of (150 – 200) psi , (200 – 250) psi and (250-300) psi respectively.

Table 5.0 shows the general reservoir properties, initial conditions used in building the model. Figure 6.4 shows the 3D view of the reservoir system used for the simulation studies. The reservoir has a variable thickness scheme for all the blocks and variable block dimensions with a single layer in the Z direction.

Table 5-0. Reservoir properties and simulation parameters

Parameter	Value
Reservoir dimensions (ft)	2725 × 1500
Number of grid blocks in x, y and z directions	12×8×1
Reservoir thickness (ft)	10
Fracture porosity, Matrix porosity (%)	1, 8
Fracture permeability, Matrix permeability (mD)	0.001, 8
Fracture spacing (ft)	1
Reservoir temperature (F)	80
Reservoir Depth (ft)	1000
Initial reservoir pressure (psia)	500
Coal density (g/cc)	1.435
Initial water saturation (fracture) %	100
Initial water saturation (matrix) %	5
Langmuir pressure constant (1/psi)	0.00597015
Langmuir volume (scf/ton)	480
Desorption time (days)	100
No of producers	1
Sandface pressure (psia)	15 psia
Well radius (ft) , skin factor(dimensionless)	0.25 , 0

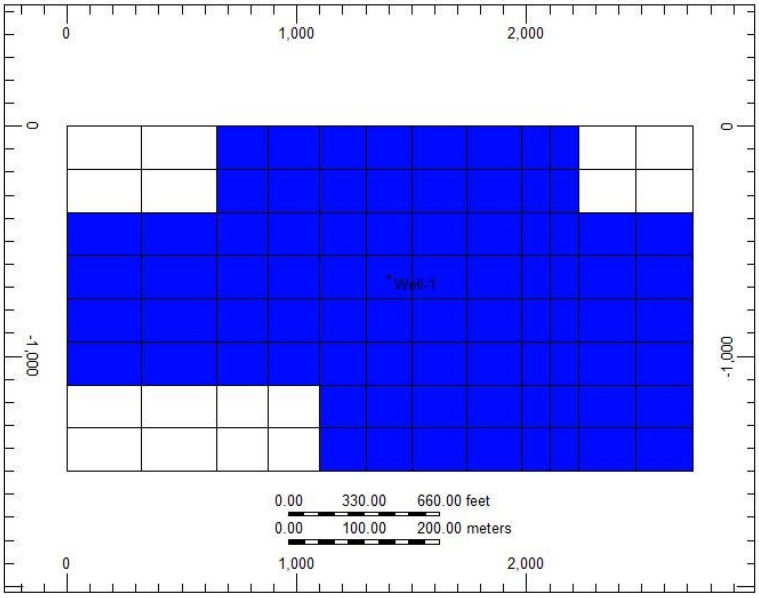

Figure 6-4. Areal view of the reservoir system used in the simulation studies

Figure 6.5 shows the comparison between gas production rates from Case 1 to Case 5. As can be seen, the predicted gas production rate is the highest for the X –type relative permeability curve formulation. This is followed by the gas rate obtained by using the experimentally obtained set 1 kr's which is followed by set 2 and 3 respectively. Case 2 represents the gas production obtained by using the kr's which is predominantly used in commercial CBM simulators (Law et al., 2002). The production generated by Case 2 falls somewhere in between Cases 1,3, 4 and 5. Figure 6.6 shows the associated cumulative gas production comparisons. The individual curves represented in Figures 6.5 and 6.6 were obtained by assuming that the relative permeabilities remain constant throughout the entire production period which is the conventional approach.

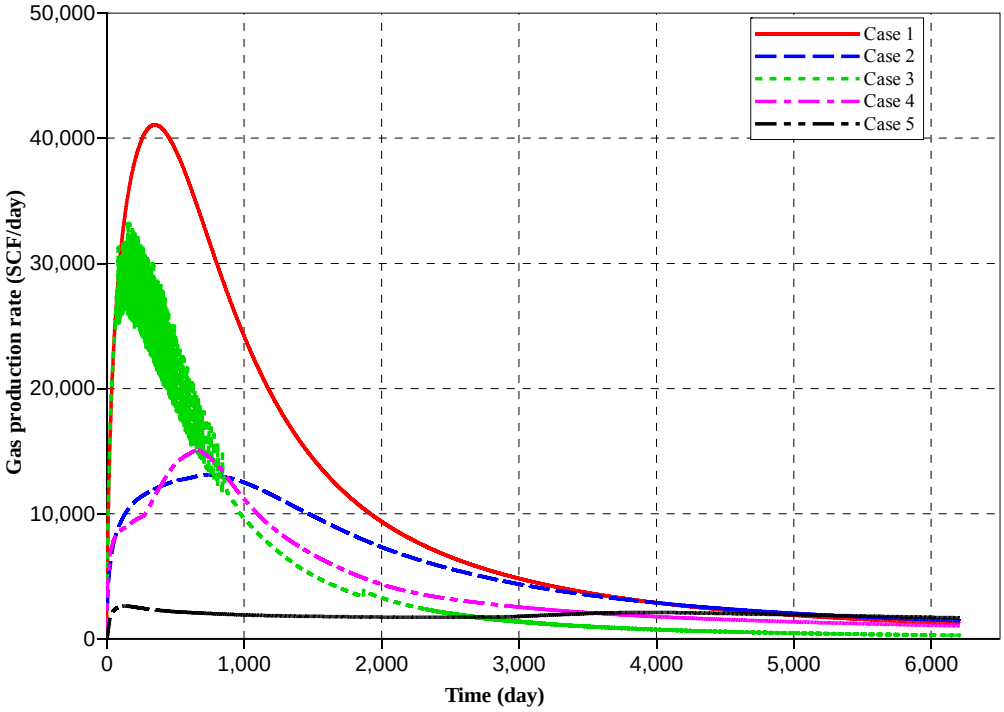

Figure 6-5. Gas production rate comparisons for different cases described in Table 4.5

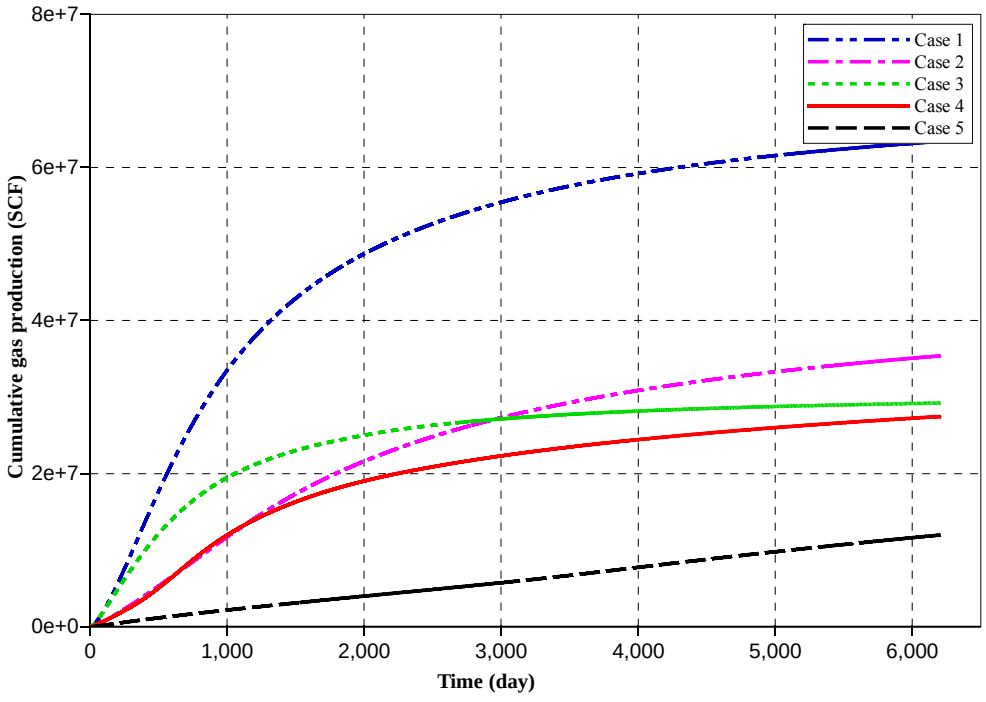

Figure 6-6. Cumulative gas porduction for different cases described in Table 4.5

The net stress acting on a reservoir changes with time and depletion. To bring into perspective the effect of net stress on the movement of gas and water in coal fractures, different relative permeability relationships were used. To use the relative permeability relationships described in Tables 4.7, 4.8 and 4.9, times at which the effective reservoir pressure fell between the effective stress ranges associated with the relative permeability curves was identified from a base simulation by using the relative permeabilities described by Table 4.6. Since the experimentally obtained relative permeability relationships start from an effective stress range of 150 psi, it was assumed that from time zero to the time at which the effective reservoir pressure became 150 psi, the depletion can be described by the relative permeabilities described by the description given in Table 4.6. Table 5.1 shows the time, the corresponding average reservoir pressure at that time and the type of relative permeability relationships used.

Figure 6.7 shows a comparison between the cumulative gas production obtained by using single and multiple relative permeability relationships (case 6). As seen, the cumulative gas production obtained by using multiple or stress dependant relative permeability curves is less in comparison to the production generated by the use of one single relative permeability relationship for the entire period of production.

Table 5-1. Description of relative permeability curves usage based on time and effective reservoir pressure

Time (days)	P_{avg} (psia)	P_{eff} (psia)	P_{eff} range (psia)	Relative permeability description
0	500	0	0	--
761	350	150	0-150	Table 4.6
1064	300	200	150 -200	Table 4.7
1430	250	250	200 - 250	Table 4.8
1946	200	300	> 250	Table 4.9

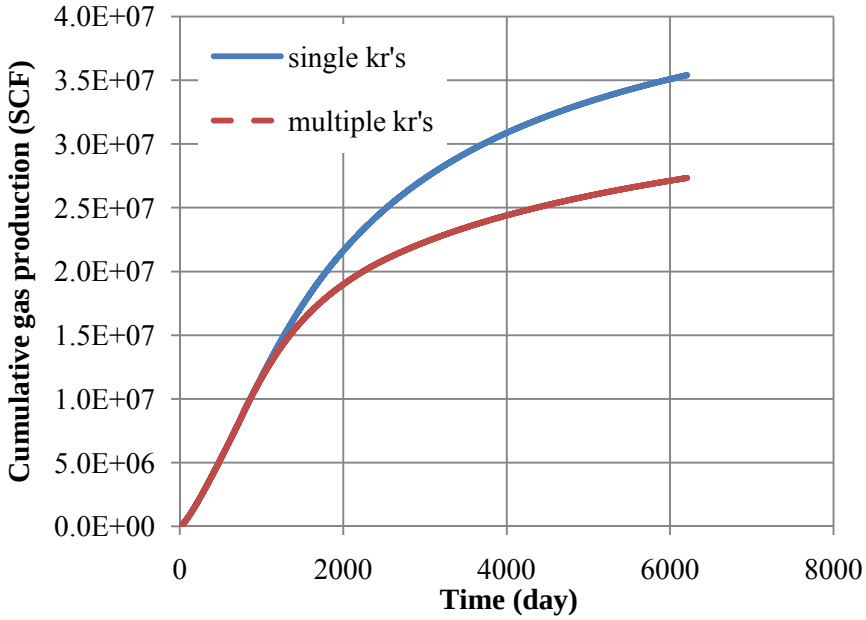

Figure 6.7 Cumulative gas production: comparison between using single and multiple kr's

The cumulative gas production decline curve (dotted) starts to deviate from the other curve at the time when the first experimentally obtained relative permeability curve is used at the end of 1064 days when the effective reservoir pressure is between 150 and 200 psi. Similarly different relative permeability relationships are used as described in Table 5.1 depending when the effective reservoir pressure falls in between the specified ranges.

Chapter 6

CONCLUSIONS AND INSIGHTS

- An improved steady state experimental technique that enables one to inject brine and gas in a closed circulation loop has been implemented to measure the absolute and relative permeability of coal samples. Reaching steady state and maintaining the steady state is critical as the steady state conditions have to be maintained until the X-ray CT scanning of the sample is completed. With this approach it is possible to reach steady state for the set of injection flow rate of fluids within a reasonable amount of time.
- The exponential trend of the decline of permeability with effective stress is an indication that permeability (or the absolute cleat permeability) is a function of overburden stress as demonstrated by several other researchers (Saites et al., 2006; Guo et al., 2008). We observe with time and repeated experimentation, this observed decline behavior becomes less evident and at some point the change in permeability becomes independent of effective stress.
- Since absolute fracture permeability of the sample has been seen to vary and decrease with time, a methodology for conducting two-phase flow tests in coal samples is proposed. Measuring the absolute permeability before two-phase flow test and after the two phase flow test can mark the limits of the absolute permeability variation. Then, for calculating relative permeabilities the absolute base permeability that has to be used for dividing the effective permeability of the phases can be an average of the permeability obtained using the two extreme limits chosen at the particular effective stress that is measured during the two phase flow test. In this way, one can obtain the relative

permeabilities of coal to the flowing phases by using the relevant effective permeabilities and absolute permeability of the system.

- As the confining stress increases, the mobile two phase flow region decreases and the irreducible water saturation increases as observed from effective permeability measurements at different confining pressures.
- Increase in confining pressure changes the relative and effective permeability of coal to gas and water and at higher confining pressures the effective permeabilities and the relative permeabilities are smaller. The change in effective permeability to water at different confining pressure conditions is more significant in comparison to the change in effective permeability to gas due to water blockage.
- As the effective stress increases, the effective permeability of coal to gas and water decreases and in general are depressed when compared to conventional reservoirs. The lowest effective permeabilities are observed at the highest effective stress and the relative change in the effective permeabilities are more pronounced for the water phase in comparison to the gas phase as we move from one range of effective stress to the other.
- In the CO_2-brine experiments, based on the measured effective permeabilities and the corresponding effective stresses, one was able to attribute the reduction in permeability of coal to gas and water to swelling caused by sorption effects
- Simulation studies have shown the recovery of predicted gas recovery is primarily affected by the stress dependent relative permeability relationships provided as inputs to the reservoir model
- The concept of using multiple relative permeability relationships depending on the effective stress regime in CBM reservoir models can affect the recovery of gas to different extents and the effect may be significant. However more modeling studies with the implementation of the proposed approach has to be carried out to test the significance

of the approach. This approach can be more suitable as no more we rely on one particular set of relative permeability relationships that is assumed to be constant during the entire producing life of stress sensitive reservoirs like coal bed methane reservoirs

- Based on the influence of effective stress on the flow of gas and water in coal fractures, these observations can be tied to a mechanistic description of two-phase flow behavior linked to changes in fracture aperture or the specific surface area of the aperture. More experimental studies are needed to demonstrate this.

Fracture volume compressibility is one of the major factors affecting the permeability/ relative permeability of coal to gas and water. When the sample undergoes repeated application and removal of external stress, there will be compaction and dilation of the cleat network and some parts of the sample could experience permanent cleat width reduction thus affecting the permeability of the cleat system.

Due to the application of overburden stress, coal can undergo plastic deformation depending when the elastic limit of the coal is exceeded and this could permanently change the arrangement of the matrix and the cleat network structure thereby affecting the permeability.

The interfacial tension between gas and liquid, gas and solid and liquid and solid also affects the transport of the flowing phases in the presence of each other. When gas and water phases are flowing simultaneously, if the fracture width is small enough to have a thin film of liquid, the movement of gas can be hindered as gas can be flowing as a dispersed phase inside the continuous liquid phase. This could be a reason for the consistence observation of the effective permeability of gas and water being much less than the prevailing absolute permeability of the sample at that point in time. The irregularity of the fracture surfaces and roughness can also affect the movement of the flowing phases.

Changing temperature conditions can affect the fluid properties during multiphase flow which can affect their transport in the presence of each other which. Additionally the presence of minerals bound to the fracture surfaces can interact with the changing fluid properties with temperature to affect their individual permeabilities

Solubility of CO_2 in brine could affect the pH of the dense phase which could alter the transport mechanisms in the presence of minerals in the fractures

At the field scale in a CBM reservoir, depending on the nature of the coal and its associated maceral composition, the affinity for that particular coal seam to retain water can be high or low. This could indicate that although the flow is predominantly single phase after dewatering, certain regions of the coal seam may still retain significant amounts of water impeding gas transport in the presence of water

Although the present study addresses fluid flow in coal fractures, the contributions of diffusion and sorption mechanisms occurring in the coal matrix cannot be entirely decoupled when formulating the relative permeability relationships for fractures as adsorbing gases like CO_2 is transported through coal by a combination of viscous and diffusion mechanisms.

Future Work

As observed from the relative permeability experiments, the behavior of effective permeabilities to gas and water indicate that the effective and relative permeability relationships can be represented as a surface instead of being a function of saturation alone. The changes in the specific surface area of the fracture network in response to the changes in effective stress could be more suitable as the second variable to relate relative permeabilities as multi-dimensional functions. By obtaining better resolution CT images, the changes in specific surface area can be mapped and can be related to the multiphase flow characteristics happening in the fracture network.

By conducting simple sorption experiments with and without moisture content in fracture network and relating the changes in coal fracture network in response to sorption with the use of X-ray CT scanning will aid in understanding how the fracture network responds to swelling/shrinkage and visually identify the heterogeneous structural changes in the sample. With this information and with the use of subsurface imaging to identify existing cleat connectivity patterns in the coal seam, it might be possible to drill wells in regions where swelling will be minimal to obtain maximum injectivity during an ECBM process. Especially using CO_2 and a mixture of methane can identify how they compositely affect the adsorption process which could reflect the true adsorption/desorption process and how they tie to the fracture network changes

During a ECBM process, several species exist in downhole conditions, like CO_2, CH_4 , N_2, H_20. In conventional reservoir modeling of CBM reservoirs, a single relative permeability relationship is used to model the two phase flow behavior. Conducting experiments with the use of a mixture of gases and brine will help to simulate the actual conditions and based on the results

obtained we can see whether there is any difference in the relative permeability curves obtained using separate species of gases along with brine.

Injection of supercritical CO_2 could change the wettability of coal as observed by (Mazumdar et al., 2003). Relative permeability studies using brine and CO_2 in the supercritical state could be compared against the multiphase flow characteristics of gaseous CO_2 to observe the changes needed in the two phase flow description

REFERENCES

Aslan, E. 2013. Development and Testing of Advanced Coalbed Methane Numerical Reservoir Simulator. PhD Thesis, The Pennsylvania State University, University Park, PA 16802.

Clarkson, C.R., Rahamanian, M.R., Kantzas, A and Morad, K.1998. Relative Permeability of CBM reservoirs: Controls on Curve Shape. SPE 137404, Canadian Unconventional Resources and International Petroleum Conference, Calgary, Canada, 19 – 21 Oct

Connell, L.D., Meng, L., and Pan, Z. 2010. An analytical coal permeability model for tri-axial strain and stress conditions. International Journal of Coal Geology, v. 84, pp. 103-114.

Dabbous, M.K., Reznik, A.A., Taber, J.J., and Fulton, P.F. 1973. The Permeabillity of Coal to Gas and Water. SPE Reprint Series, No.35: Coalbed Methane, SPE Richardson, Texas,1992,pp. 46 – 55

Denison, C., and Carlson, W.D., 1997. Three-dimensional quantitative textural analysis of metamorphic rocks using high-resolution computed X-ray tomography: Part II. Application to natural samples. Journal of Metamorphic Geology, v.15, no. 1, pp.. 45–57

Duan, Y., Meng, Y., Luo, P., and Su, W.1998. Stress Sensitivity of Naturally Fractured-porous Reservoir with Dual Porosity. SPE 50909, SPE International Conference and Exhibition, Beijing, China, 2-6 Nov

Ertekin, T., and Sung, W.1989. Pressure Transient Analysis of Coal seams in the Presence of Multi-Mechanistic Flow and Sorption Phenomena. SPE 19102, SPE Gas Technology Symposium, Dallas, TX, 7-9 Jun

Ertekin, T., W. Sung, and F. C. Schwerer. 1988. Production Performance Analysis of Horizontal Drainage Wells for the Degasification of Coal Seams. J. Petroleum Technology, v. 40, no. 4, pp.625- 632

Gash, B. 1991. Measurement of “Rock Properties” in Coal for Coal Bed Methane Production. SPE 22909, SPE Annual Technical Conference and Exhibition, Dallas, TX, 6-9 Oct

Gash, B.W., Volz, F.R., Potter, G., and Corgan, J.M., 1992. The Effects of Cleat Orientation and Confining Pressure on Cleat Porosity, Permeability and Relative Permeability in Coal. Paper 9224, The Society of Core Analysts Conference, Tulsa, Oklahoma, June

Guo, R., Manhardt, K.., and Kantzas, A..2008. Laboratory investigation on the Permeability of Coal During Primary and Enhanced Coalbed Methane Production. Journal of Canadian Petroleum Technology, v 47, No.10, pp. 27-32

Gray, I., 1987. Reservoir engineering in coal seams, part 1—the physical process of gas storage and movement in coal seams. SPE Reservoir Engineering , vol 2 , No .1,pp. 28–34.

Hall, F.E., Chunhe, Z., Gasem, K.A.M., Robinson, R.L., Yee,D., 1994. Adsorption of pure methane, nitrogen and carbon dioxide and their binary mixtures on wet fruitland coal. Paper SPE 29194, Eastern Regional Conference and Exhibition, Charleston, West Virginia, Nov. 8 – 10

Ham., Y.S., and Kantzas, A., 2011. Relative Permeability of Coal to Gas and Water – Results and Experimental Limitations. Petroleum Society's Canadian Unconventional Resources Conference, Calgary, Alberta, Canada, Nov. 15- 17

Harpalani, S., and Shraufnagel,A., 1990. Measurement of parameters impacting methane recovery from coal seams. International Journal of Mining and Geological Engineering, 8, pp. 369 – 384.

Harpalani, S., Chen, G., 1995. Estimation of changes in fracture porosity of coal with gas emission.Fuel,vol 74, No.10, pp. 1491–1498.

Hassanizadeh, S.M. Gray, W.G., 1993a. Thermodynamic basis of capillary pressure in porous media. Water Resour. Res., 29, 3389–3405.

Honarpour, M.M., Koderitz, L., and Harvey, A.H.1986. Relative Permeability of Petroleum Reservoirs, CRC Press, Boca Raton, Florida, USA. ISBN 0 -8493-5739-X

Hyman, L.A., Brugler, M.L., Daneshjou, D.H., and Ohen, H.A., 1992. Advances in Laboratory Measurement Techniques of Relative Permeability and Capillary Pressure for Coal Seams. Quarterly Review of Methane from Coal Seams Technology , Jan, pp. 9 -16.

Joekar-Niasar, V., Hassanizadeh, S.M., Leijnse, A. Insights into the Relationships Among Capillary Pressure, Saturation, Interfacial Area and Relative Permeability Using Pore-Network Modeling Transport in Porous Media, 2008, 74(2), 201–219.

Johnson, E. F., Bossler, D. P., and Naumann, V. 0. 1959. Calculation of Relative Permeability from Displacement Experiments. Transactions of the AIME, 216, pp. 370-372.

Jones, A.F., Bell, G.J., Taber, J.J., and Schraufnagel, R.A., 1988. A Review of the Physical and Mechanical Methane Properties of Coal with Implications for Coal – Bed Methane Well Completion and Production. Coal Bed Methane, San Juan Basin, Rocky Mountain Association of Geologists, pp. 169- 182

Jones, C., Al- Quraishi, A.A., Somerville, J.M., and Hamilton, S.A.2001. Stress sensitivity of saturation and end-point relative permeabilities. Oral presentation SCA 2001 -11, International Symposium of the Society of Core Analysts, Edinburgh, Scotland, Sept. 17 -19.

King, G. R., T. Ertekin, F. C. Schwerer. 1983. Numerical Simulation of the Transient Behavior of Coal-Seam Degasification Wells. Paper SPE 12258, SPE Reservoir Simulation Symposium, San Francisco, California, Nov.

Law, D. H. -S., van der Meer, L. G. H. and Gunter, W. D.2002. Numerical Simulator Comparison Study for Enhanced Coalbed Methane Recovery Processes, Part I: Pure Carbon Dioxide Injection. Paper SPE 75669, SPE Gas Technology Symposium, Calgary, Alberta, Canada, 30 April–2 May.

Levine, J.R., 1996. Model study of the influence of matrix shrinkage on absolute permeability of coal bed reservoirs. Geological Society, London, Special Publications 109 (1), pp. 197–212.

Lian, P.Q., Cheng, L.S., and Ma, C.Y. 2012, The Characteristics of Relative Permeability Curves in Naturally Fractured Carbonate Reservoirs. Journal of Canadian Petroleum Technology, V 51, No.2, pp.137-142

Manik, J., T. Ertekin, T. E. Kohler. 2000. Development and Validation of a Compositional Coalbed Simulator. Paper No.2000-44, Petroleum Scoiety's Canadian International Petroleum Conference ,Calgary, Alberta, Canada. June

Mazumdar, S., Plug, W-J., and Bruining, H., 2003. Capillary Pressure and Wettability Behavior of Coal –Water-Carbon dioxide system. Paper SPE 84339, SPE Annual Technical Conference and Exhibition, Denver, CO, Oct. 5-8.

Katyal, S., Valix, M., Thambimuthu, K., 2007. Study of Parameters Affecting Enhanced Coal Bed Methane Recovery. Energy Sources, Part A, 29, pp. 193 -205

King, G. R., T. Ertekin, F. C. Schwerer.1983. Numerical Simulation of the Transient Behavior of Coal-Seam Degasification Wells. Paper SPE 12258, SPE Reservoir Simulation Symposium, San Francisco, California, Nov.

Olsen, T.N., Brenize, G., and Frenzel, T. 2003. Improvement Processes for Coalbed Natural Gas Completion and Stimulation.Paper SPE 84122 presented at the SPE Annual Technical Conference and Exhibition, Denver, Colorado, 5–8 October.

Palmer, I., and Mansoori, J.1996. How Permeability Depends on Stress and Pore Pressure in Coalbeds: A New Model. Paper SPE 36737, SPE Annual Technical Conference and Exhibition, Denver, Colorado, U.S.A., 6-9 October.

Pan, Z., Connell, L.D. and Camilleri, M.2010. Laboratory characterization of coal reservoir permeability for primary and enhanced coalbed methane recovery. International Journal of Coal Geology, v 82, pp. 252-261

Paterson, L., Meaney, K., and Smyth, M.,1992. Measurement of Relative Permeability, Absolute Permeability and Fracture Geometry in Coal. Coalbed Methane Symposium, Townsville, Queensland, Australia, 19 – 21 Nov.

Pekot, L.J., and Reeves, S.R..2003. Modeling the effects of matrix shrinkage and differential swelling on coalbed methane recovery and carbon sequestration, Proceedings of the International Coalbed Methane Symposium, Tuscaloosa, Alabama, U.S.A., May 5-7

Persoff, P., and Pruess, K. 1995. Two-Phase Flow Visulaization and Relative Permeability Measurement in Natural Rough-Walled Rock Fractures. Water Resources Research, v 31 , No.5, pp. 1175-1186.

Piri, Mohammad. 2012. Recirculating, constant back pressure core flooding apparatus and method. US Patent 20120211089 A1, filed Dec, 13 2011, and issued Aug 23, 2102

Puri, R., Evanoff, J.C., and Brugler, M.L., 1991. Measurement of Coal Cleat Porosity and Relative Permeability Characteristics. SPE Gas Technology Symposium, SPE 21491, Houston, Texas, 23 – 25 Jan

Reznik, A.A., Dabbous, M.K., Fulton, P.F. and Taber, J.J.1974. Air-Water Relative Permeability Studies of Pittsburgh and Pocahontas Coals. SPE Journal, v 14, No.6,pp.556-562

Robertson, E.P., Christiansen, R.L., 2007. Modeling laboratory permeability in coal using sorption-induced strain data. SPE Reservoir Evaluation and Engineering, vol 10, No. 3,pp. 260–269.

Saites, F., Wang, G., Gou, K., and Kantzas, A. 2006. Coalbed Characterization Studies With X-Ray Computed Tomography(CT) and Micro CT Techniques. Canadian International Petroleum Conference, Calgary, Alberta, Canada, June. 13- 15.

Seidle, J. P. and Huitt, L. G, 1995. Experimental Measurement of Coal Matrix Shrinkage Due to Gas Desorption and Implications for Cleat Permeability Increases. Paper SPE 30010, International Meeting on Petroleum Engineering, Beijing, PR China, Nov 14- 17.

Seidle, J.P., Jeansonne, M.W., and Erickson, D.J. 1992. Application of Matchstick Geometry to Stress Dependent Permeability in Coals. Paper SPE 24361, SPE Rocky Mountain Regional Meeting, Casper, Wyoming, May 18- 21.

Shedid, A.S., and Rahman, K.2009. Experimental Investigations of Stress-Dependant Petrophysical Properties and Reservoir Characterization of Coalbed Methane (CBM). Paper SPE 120003, SPE Asia Pacific Oil and Gas Conference Exhibition, Jakarta, Indonesia, Aug. 4- 6.

Shen, J., Qin, Y.,Wang, G,X., Fu, X., Wei, C., and Lei, B.2011. Relative permeability of gas and water for different rank coals. International Journal of Coal Geology, 86,pp 266-275.

Shi, J. and Durucan, S., 2005. A Model for Changes in Coalbed Permeability during Primary and Enhanced Methane Recovery. SPE Reservoir Evaluation and Engineering, August.

Thararoop, P., Karpyn, Z. T., Ertekin, T., 2009. Development of a coal shrinkage-swelling model accounting for water content in the micropores. International Journal of Mining and Mineral Engineering, vol. 1, no.4, pp. 346-364

Warpinski, N.R. 1991. Hydraulic Fracturing in Tight Fissured Media , SPE 21054, Journal of Petroleum Technology, v 43, No. 2, pp. 146-152 and 208-209.

Appendix

Coal Petrography and Proximate Analysis

A basic coal characterization including proximate analysis (volatile matter, fixed carbon and ash), total sulfur and petrographic analysis (mean maximum vitrinite reflectance and maceral analyses) were carried out on the coal samples used in this study. The petrographic analysis for which the procedure, results are given below was performed at the Organic Petrology Laboratory, Energy Institute, Pennsylvania State University. The proximate analysis was carried out at CoalTech Petrographic Associates, Murrysville, PA

Procedures

Stage crushing and riffling were performed on each sample to reduce particle size range, mass and to obtain representative subsamples. Aliquots suitable for proximate (volatile matter, ash and fixed carbon) plus total sulfur and petrographic analyses (mean maximum vitrinite reflectance and maceral composition) were obtained according to appropriate ASTM test methods (Annual book of ASTM standards, 2012). Arrangements were made to send minus 60 mesh (0.25 mm) subsamples for proximate and total sulfur analyses to CoalTech Petrographic Associates, PA whereas several minus 20 mesh (0.85 mm) subsamples were separated for preparation of samples for petrographic analysis and for a small amount of reserve.

Preparation of standard petrographic briquettes begins with about 50g of minus 20 mesh coal, mixed with sufficient cold-setting epoxy resin to wet the coal particles. Two steel molds with end caps were filled with the coal-epoxy mixture and pressed to 4,000 psi for three minutes and allowed to harden overnight. The cylindrical samples were removed from the molds and one end ground (400 and 600 grit) and polished (0.3 μm and 0.05 μm alumina slurry on a

high-nap cloth and silk, respectively). Freshly polished briquettes were stored over a desiccant overnight to eliminate interference of water with the immersion oil used during microscopy.

Because some bituminous coals release oils or bitumens that can dilute immersion oil changing its' index of refraction, general petrographic procedures require that reflectance measurements be carried out immediately after a brief qualitative characterization of the coal surface. Mean maximum vitrinite reflectance (Rmax) was employed to assess the relative maturity of the coal organic matter as an independent method free of the influence of composition. Using the ASTM test method (D2798) with a Leitz MPV2 photometric research microscope, the photomultiplier current was adjusted into the range of reflectance of the coal using optical glass standards. Once the microscope system was standardized and stabilized reflectance values were collected following a grid-like pattern in which reading were taken on the next available vitrinite particle after 1.0 mm of traverse.

For this test light reflected from vitrinite surfaces passes through a 546 nm interference filter and a 3 μm spot of incident light is impinged on the photomultiplier cathode to generate a current. The microscope stage/sample is rotated through 360° to determine the greatest reading from each particle. For a normal coal 100 reading, 50 on each of two briquettes are recorded and the mean value reported. The repeatability of these analyses is good to within 0.02 % and the reproducibility is good to within 0.06 % between replicate analyses.

In this analysis, the mean Rmax and standard deviation are reported in Table A1 and the distribution of readings on a 0.05 interval are compared for each core segment in Figure A1. Furthermore, the percentages of reflectance reading taken in each 0.1 reflectance interval, known as vitrinite-types or V-types, are used to divide the vitrinite population into increments. The technique is useful in defining the relative thermoplasticity and reactivity of coals as well as determining the complexity of coal samples, i.e., most single seam coals will have reflectance values that cover three V-types.

A Zeiss Universal research microscope with a vertical illuminator capable of delivering polarized light to the polished surface at 625X magnification was used for maceral analysis. The ASTM provides a standard method to quantify the volume percentage of the physical components of coal (D2799) using a specific list of macerals suitable for the characterization of coals of bituminous rank and greater. Lower rank coals (lignite and subbituminous) can be characterized using this technique or by using brown coal terminology as covered by the International Committee for Coal & Organic Petrology (International Handbook of Coal Petrology, 1971). However, the technique described in the ASTM standard (D2799) is applicable to both terminologies and covers the equipment and procedures used for determining the physical composition of coals. The macerals specifically identified and defined in the standard, include; undifferentiated vitrinite, the liptinite group macerals of sporinite, resinite, cutinite, liptodetrinite, and alginite, and the inertinite-group macerals of fusinite, inertodetrinite, macrinite, micrinite, semifusinite and funginite. In addition to this terminology it may be useful to know the distribution of the individual vitrinite macerals as provided by the International Committee for Coal and Organic Petrology (1998) including telovitrinite macerals, those containing remnant cellular structures, of telinite and collotelinite; detrovitrinite macerals, those containing fragments and degradation products of vitrinite, of vitrodetrinite and collodetrinite; and gelovitrinite, those that were derived from a gelatinous source, of corpocollinite and gelinite.

Maceral analysis is based on point counting in which the volume percentage of different randomly distributed materials may be estimated by counting their occurrence in two dimensions. For this evaluation the polished coal surface was traversed in a regular grid of 0.6 x 0.6 mm between points and lines. At each interval, a coal maceral appearing under the microscope eyepiece crosshair is identified and counted. Measurements of 500 counts on each of two polished briquettes were taken for a total of 1000 counts and the percentage of each maceral determined on a mineral matter free basis; counts on the epoxy binder and on mineral matter were

ignored. The Parr formula shown below may be used to calculate the volume basis mineral matter from the weight percent of ash and total sulfur values (dry basis). Results for compositional analyses are shown in Table A1 & A2.

Mineral Matter, % = [[(1.08A+0.55S)/2.8]100]/[100 - (1.08A+0.55S)]/[1.35 + (1.08A+0.55S)/2.8], where A = Ash and S = Total Sulfur, on a dry basis

Results

In general, the coal samples can be classified as high volatile A bituminous rank based upon mean maximum reflectance being in the range of 0.71-1.10% for US coals although these samples are in the rank range that requires determination of calorific value (mineral matter free basis) to classify properly. Figure A1 compares the reflectance distributions of all samples demonstrating their relative uniformity. A check of the Penn State Coal Database shows that coals of similar reflectance (0.74-0.77%), vitrinite content and ash yield have volatile matter in the range of 39.92 – 46.14 % on a daf basis compared with the mean value (44.88%) derived from the three samples being evaluated (Table A1).

In terms of composition there are trends showing decreasing vitrinite concentration with increasing liptinite and inertinite macerals from sample #2 to #3 to #4 (Table A1). Because of this sample #2 was the brightest, most vitreous of the group, while samples #3 and #4 were duller owing to the decrease in vitrinite and increasing inertinite and mineral content. As shown in Tables A1 & A2, vitrinite group macerals were the most common observed, being largely represented by collotelinite with decreased contributions of vitro- and collo- detrinite. From the high concentration of vitrinite and the similar fossil leaves (shown in Figure A2) observed in all three samples suggested a fairly stable environment occupied by the same population of plants.

Ash yield (Table A1) increased nearly three-fold from sample #2 to #4 and a significant change in mineralogy was observed as well. During petrographic analysis minerals from four basic groups were found, but it is difficult to be precise about their relative concentrations among

sample. In general, clay minerals (illite observed) accounted for a large fraction of the minerals in all samples including those dispersed within the vitrinite matrix, found as thin layers and lenses, as infilling in other macerals and as the matrix of shale particles derived from large (>1mm) partings. Larger shale particles were most common in sample #4 with decreasing amounts in samples #3 and #2.

Pyrite was found in high concentration and in just about every conceivable habit (euhedra, subhedra, framboids, small & large blebs, dendrites and cleat & maceral infillings) in sample #3 thereby explaining its high total sulfur content (Table A1). Sample #4 also possessed pyrite in most habits, but in much lower concentration, whereas sample #2 possessed a less diverse population composed mostly of the smaller particle types. Most of the larger types of pyrite and the cleat & infillings appear to have developed during coalification, while the framboids and crystalline forms may have been formed during or shortly after deposition.

Carbonate minerals also were observed in relatively high concentration in sample #3 as small (<70 μm diameter) multi-crystalline concretions and as cleat and maceral infillings. The cleat and infilling carbonate minerals are probably calcite ($CaCO_3$), but the concretionary carbonate particles are most likely composed of siderite ($FeCO_3$). However, while the cleat and infilling carbonates were from secondary mineralization the concretions were deposited with the organic matter. Regarding the other samples, only a very minor amount of carbonate was observed in sample #4, while all the carbonate habits were observed in sample #2, but in low concentration.

Small (<5μm) rounded quartz particles were observed in detrital layers and shale particles in all three samples, meaning that those samples having more detrital layers and shale particles would have more quartz, i.e., sample #4 > #3 >>#2.

Beyond the above observations of rank, type and grade there are those that were not made, i.e., no signs of weathering in the organic or inorganic fractions were observed, no sulfate

or iron oxides formation, there was no contamination from other coals or any other laboratory materials. As the concentration of liptinite macerals was below 5.0 vol. % , no effort was made to inspect these samples using blue-light irradiation.

Based upon reflectance values these coals have gone through bituminization and are mature with respect to oil development and migration. Because of the high concentration of vitrinite, in particular collotelinite, they should have a fairly well developed cleat that in some cases have been infilled with mineral matter (calcite and pyrite), particularly sample #3. Based upon the character of the maceral assemblages in these coal samples it does not appear that there was any substantial subareal oxidation of peat during deposition. However, there was evidence for a higher-energy depositional environment in the stratigraphic position of sample #4 as demonstrated by greater ash yield, mineral content and a higher concentration of liptinite and inertinite. Depending upon placement and thickness of shale partings, fluid communications from one band of coal to the next could have been impeded or channeled as with sample #4.

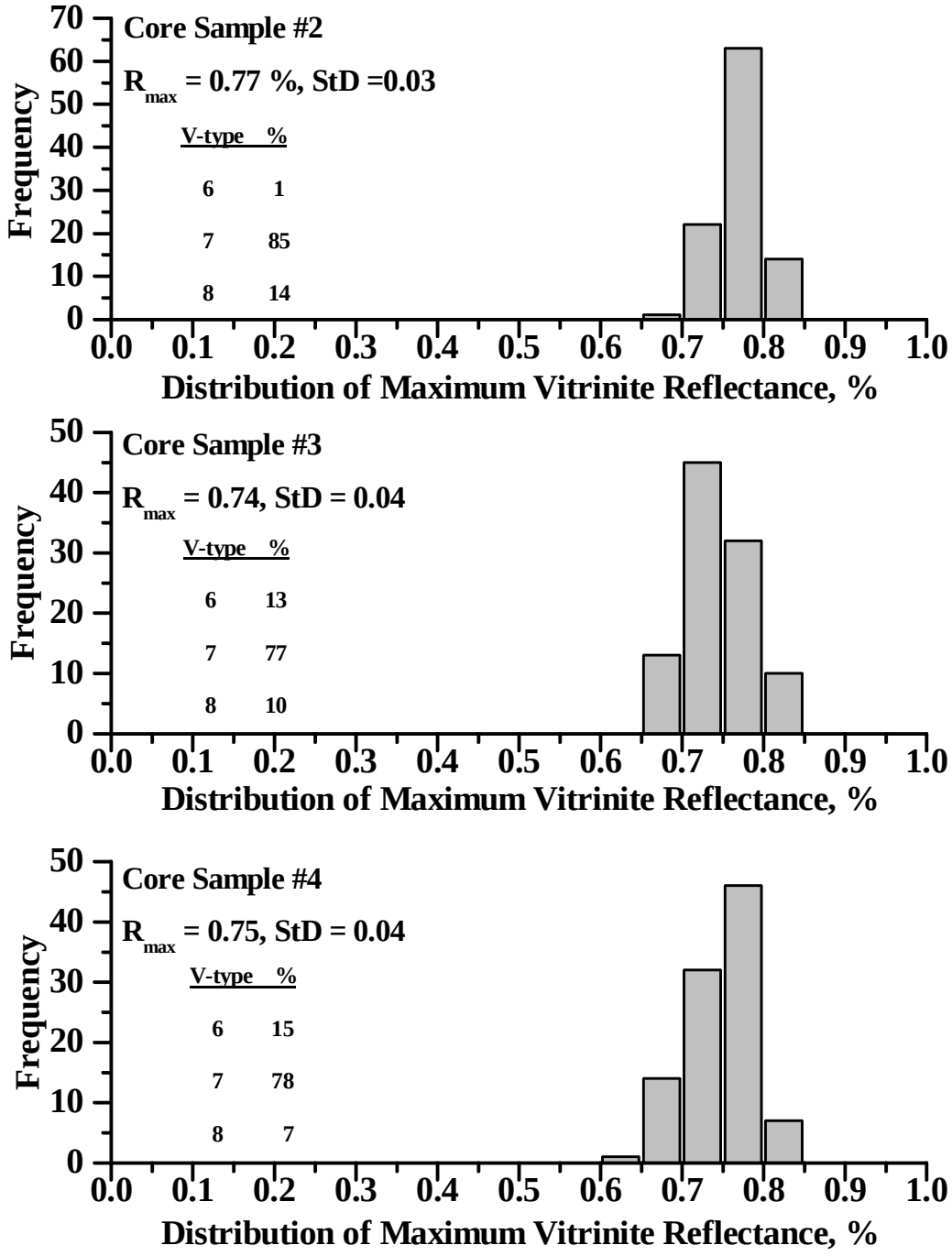

Figure A1 – Maximum Reflectance Distribution

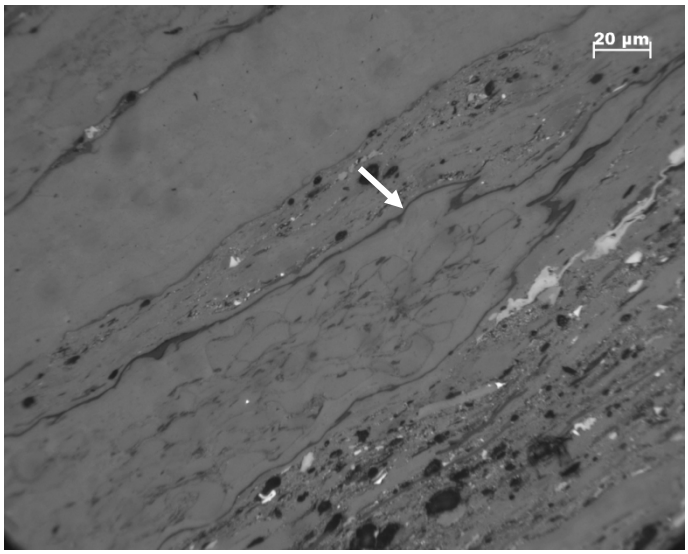

Figure A2 – Remnants of leaf structures with intact cuticle (arrow) and internal cell structures infilled with gelinite.

Table A1 – Petrographic, Proximate and Total Sulfur; Macerals vol. %, Reflectance %, All Others Wt. %

	Sample #2		**Sample #3**		**Sample #4**	
Maceral	%, mmf[a]	%, mmc[a]	%, mmf	%, mmc	%, mmf	%, mmc
Vitrinite, V-types						
6	1	1	12.1	11.4	13.1	12.1
7	81.3	78.6	71.7	67.4	67.9	63
8	13.4	12.9	9.3	8.7	6.1	5.6
Total Vitrinite	**95.7**	**92.5**	**93.1**	**87.5**	**87.1**	**80.7**
Liptinite						
Sporinite	0.4	0.4	0.8	0.8	2.6	2.4
Resinite	0.2	0.2	0.1	0.1	0.1	0.1
Cutinite	1.2	1.2	1	0.9	1	0.9
Liptodetrinite	0.4	0.4	0.2	0.2	0.6	0.6
Total Liptinite	**2.2**	**2.2**	**2.1**	**2**	**4.3**	**4**
Inertinite						
Fusinite	0.5	0.5	0.8	0.8	2.4	2.2
Semifusinite	0.5	0.5	1.9	1.8	3.9	3.6
Macrinite	0.2	0.2	0.1	0.1	0.4	0.4
Micrinite	0.6	0.6	1	0.9	0.6	0.6
Inertodetrinite	0.3	0.3	1	0.9	1.3	1.2
Funginite						
Mineral Matter[b]	-	3.2	-	6	-	7.3
Total Inertinite	**2.1**	**5.3**	**4.8**	**10.5**	**8.6**	**15.3**
Rmax, StD, n=100	**0.77 %, 0.03**		**0.74 %, 0.04**		**0.75 %, 0.04**	
Proximate + Total Sulfur: Wt. %						
	Dry	**daf[c]**	**Dry**	**daf**	**Dry**	**daf**
% Volatile Matter	41.17	44.26	39.61	45.47	36.56	44.9
% Fixed Carbon	51.85	55.74	47.51	54.53	44.86	55.1
% Ash	6.98		12.88		18.58	
%Total Sulfur	2.53		4.48		2.2	

a) mmf = mineral matter free; mmc = mineral matter containing;
b) Mineral Matter, % = [[(1.08A+0.55S)/2.8]100]/[100 - (1.08A+0.55S)]/[1.35 + (1.08A+0.55S)/2.8], where A = Ash and S = Total Sulfur, on a dry basis

c) daf = dry ash free

Table A2 – Distribution of Vitrinite Macerals; Comparison of the Core Segments, vol. %

Macerals	**Sample #2**		**Sample #3**		**Sample #4**	
	%, mmf	%, mmc	%, mmf	%, mmc	%, mmf	%, mmc
Total Vitrinite, vol. %	95.7	92.5	93.1	87.5	87.1	80.7
Telovitrinite						
Telinite	1	1	1.9	1.8	0.6	0.6
Collotelinite	55	53.2	54.6	51.3	60.3	55.9
Total Group	**56**	**54.2**	**56.5**	**53.1**	**60.9**	**56.5**
Detrovitrinite						
Vitrodetrinite	18.3	17.7	15.7	14.8	13.3	12.3
Collodetrinite	12.2	11.8	9.2	8.6	6.2	5.7
Total Group	**30.5**	**29.5**	**24.9**	**23.4**	**19.5**	**18**
Gelovitrinite						
Corpocollinite	3.9	3.8	6.6	6.2	1.4	1.3
Gelinite	5.3	5.1	5.1	4.8	5.3	4.9
Total Group	**9.2**	**8.9**	**11.7**	**11**	**6.7**	**6.2**

VITA

Dennis Arun Alexis

Dennis Arun Alexis hails from the southeastern coastal city of Chennai in India. After finishing his high school from Don Bosco Matriculation Higher Secondary School in 2001, he obtained his Bachelor of Technology degree in Chemical Engineering in 2005 from Anna University, India. He then worked as a process engineer for a period of two years at Manali Petrochemical Limited in India. He enrolled for graduate studies in Petroleum and Natural Gas Engineering in the Fall of 2007 in the John and Willie Leone Family Department of Energy and Mineral Engineering and completed his M.S degree in December 2009. He began his PhD studies from the Spring of 2010 and since then has been conducting experimental and numerical studies to evaluate the transport properties of coal. While at Penn State University, he was an active member of the student chapter of the Society of Petroleum Engineers and was twice recognized (Spring 2012 and Fall 2012) for being the most active graduate student member. He also participated in the Society of Petroleum Engineers', Regional and International Student Paper contests in 2011 and won the second place in the Master's division at the regional level. He was also given the Graduate Merit Award in Petroleum and Natural Gas Engineering in 2010. He also served as a teaching assistant for a number of graduate and undergraduate courses with most of his assistance going towards the Petroleum Engineering Capstone design course and Rock and Fluid Properties Laboratory for over three years and serving as a fulltime instructor for this laboratory for one semester. He also worked for Gaffney, Cline & Associates in the summer of 2012 as a petroleum engineering consultant and gained hands on experience in the design of reservoir models to predict hydraulic fracturing. He can be reached at dxa197@gmail.com.